Alma Mater Studiorum · Università di Bologna

Scuola di Scienze
Corso di Laurea Magistrale in Fisica del Sistema Terra

Combined analysis of C-band polarimetric radar and disdrometer data of convective and stratiform precipitation

Relatore:
Prof. Federico Porcù

Correlatore:
Dott. Pier Paolo Alberoni

Presentata da:
Lorenzo Aiazzi

Sessione II
Anno Accademico 2019/2020

Sommario

In questo studio l'obiettivo è osservare le caratteristiche della precipitazione e di verificare la qualità del dato radar in diverse condizioni meteorologiche. In particolare, si analizzano in modo combinato dei dati di due strumenti che si basano su differenti principi di funzionamento, un radar polarimetrico in banda C e un disdrometro PARSIVEL^2.

Gli osservabili radar sono confrontati con le caratteristiche e l'evoluzione microfisica della precipitazione ricavate per mezzo del disdrometro situato nella città di Bologna (a poco meno di 28 km di distanza dal sito del radar). L'analisi combinata dei due strumenti si esegue su di un dataset che si estende per 11 mesi degli anni 2019 e 2020 e che contiene eventi precipitativi sia di carattere convettivo che stratiforme.

Le prime elevazioni del radar sono soggette a rumore causato da interferenze antropogeniche, che limitano leggermente l'estensione del dataset. Le analisi mostrano un buon accordo tra la riflettività radar e quella calcolata per mezzo del disdrometro a partire dalla Drop Size Distribution (DSD). Il coefficiente di correlazione CC tra le due stime è uguale a 0.84. Queste analisi rendono possibile anche una verifica dell'algoritmo operativo di classificazione delle idrometeore sviluppato a partire dai dati radar. Inoltre, la distinzione tra precipitazione convettiva e stratiforme ricavata dai dati disdrometrici si riflette in maniera coerente sulle grandezze polarimetriche del radar: per esempio in condizioni convettive si ha una distribuzione di riflettività differenziale che picca verso valori più alti rispetto a quella stratiforme. La distribuzione convettiva ha una mediana di 1.5 dB, mentre quella stratiforme di 0.9 dB. Infine, è portato come esempio il caso studio del temporale sviluppatosi su

Bologna nel pomeriggio del 28 maggio 2019. Questo evento mostra precipitazioni di diverse intensità e di differenti tipi di idrometeore, permettendo così una verifica dei risultati precedenti e una più dettagliata analisi delle caratteristiche delle DSD.

Abstract

The aim of the present Thesis is to observe the characteristics of the precipitation and to check the quality of the radar data under different meteorological conditions. This aim is achieved through a combined analysis of the data collected by two instruments that have different operating principles. These instruments are a C-band polarimetric radar and a PARSIVEL^2 disdrometer.

Radar variables are compared with the characteristics and the microphysics evolution of the precipitation retrieved by the disdrometer. The disdrometer is located in the city center of Bologna, a little less than 28 km far from the radar site. The combined analysis of the two instruments is done for a dataset that includes 11 months of the years 2019 and 2020. The dataset contains convective and stratiform precipitation events.

The lower radar elevations are affected by anthropogenic interferences that slightly reduce the dataset extension. The analyses show a good correlation between the reflectivity factors retrieved by the radar and by the disdrometer through the Drop Size Distribution (DSD). The correlation coefficient CC between the two estimations is 0.84. These analyses also enable a verification of the operational algorithm of the hydrometeor classification obtained through the radar data. Moreover, the convective and stratiform discrimination developed through the disdrometer data is consistent with the polarimetric variables of the radar. For example, the distribution of the differential reflectivity peaks for higher values in a regime of convective precipitation in comparison to the stratiform regime. The convective distribution of the differential reflectivity has a median of 1.5 dB, while the stratiform one has

a median of 0.9 dB. Lastly, the case study of a thunderstorm occurred in Bologna on May 28th 2019 is described. This case study shows precipitation structures of different intensities and different types of hydrometeors, allowing a verification of the previous results and a more-detailed analysis of the DSD characteristics.

Contents

List of Figures

List of Tables

Introduction

The precipitation phenomenon involves all the liquid or frozen water particles originated in the atmosphere, falling to the earth's surface. The precipitation fields have a complex structure, shaped by the interplay of many mechanisms, including for example, turbulence, strong currents, and hydrometeors collision, coalescence and breakup.

Two of the most advanced instruments to study this phenomenon are the weather radar and the disdrometer. The radar is used for surveillance purposes in operational meteorology and provides remote measurements of bulk precipitation characteristics over a broad area. The disdrometer is mainly used for research purposes and it allows a more detailed knowledge of the precipitation structure, making in situ measurements of every single drop. In the present Thesis a combined analysis of radar and disdrometer data is performed, aiming to make the best out of the two instruments that have different operating principles.

This analysis allows to examine the characteristics and the evolution of rain microphysics and of different precipitation regimes. These studies find application in fields such as extreme events analysis, hydrogeological risk prevention and climate assessments. Moreover, disdrometer is used for radar calibration which is important, having consequences on the environment and the human activities due to the radar

monitoring and surveillance role.

In this work, radar and disdrometer datasets are preprocessed and matched. Firstly, retrieved values of reflectivity factor, which depends on particles size distribution, are compared discussing different approaches and techniques. Then, disdrometer data are used to discriminate between convective and stratiform precipitation regimes. The first one is associated to intense and localized rain that sometimes comes with solid particles; the other is characterized by lighter and more uniform rain intensity. Therefore, the distributions of the radar variables in the two precipitation regimes are studied. The precipitation classification (rain, snow, hail, ...) achieved by the two instruments is also analyzed and in conclusion a case study of a thunderstorm event is investigated in details.

This Thesis includes four chapters.

Chapter 1 illustrates the background physical theory of the precipitation phenomenon and describes instruments principles and operations.

Chapter 2 introduces the characteristics of the instruments used in the present work and related datasets. The chapter continues with the description of filters applied to the datasets and samplings matching procedure.

Chapter 3 illustrates the analysis accomplished and the achieved results.

In Chapter 4 the results of the present Thesis are discussed.

Chapter 1

Theory of precipitation and precipitation measurement

In this chapter the physical properties of the precipitation are introduced; then, the instruments for precipitation measurement are presented, focusing on radar and disdrometer characteristics. In Section 1.1 the formation of clouds, the different types of hydrometeors and the precipitation process are described, making distinction between convective and stratiform precipitation regimes. In Section 1.2 the precipitation variables are introduced and in addiction it is defined the Drop Size Distribution (DSD), that is a quantity linked to the characteristics of the precipitation. Section 1.3 summarizes the instruments used to measure precipitation, then in Sections 1.4 and 1.5 the description focuses on radar and disdrometer.

1.1 Precipitation

Precipitation is defined by the American Meteorological Society (AMS) as "all liquid or solid phase aqueous particles that originate in the atmosphere and fall to the earth's surface".

The particle formation is a consequence of the vertical displacement of humid air masses. These masses upward movement is driven by thermal and/or dynamic forcing and causes in the adiabatic approximation the air expansion and cooling. In the ascent the air reaches certain values of saturation, following the Clapeyron–Clausius equation, and the cloud droplets start to form through the condensation process.

Two hydrometeor formation processes exist: homogeneous and heterogeneous nucleation, where the term "nucleation" represents the initiation of a phase change of a substance to a lower thermodynamic energy state. Homogeneous nucleation needs high values of supersaturation, that is the condition when air contains more water vapor than is needed to produce saturation with respect to a plane surface of pure water or pure ice (AMS glossary). These high values are never reached in real atmosphere, because it contains a sufficiently large amount of particles ("condensation nuclei") that act like a substrate for nucleation at low supersaturation values. This is the case of heterogeneous nucleation and when it occurs the cloud forms.

When the droplets reaches temperature below $0^\circ C$, they are defined "supercooled", which is the condition where droplets are in liquid state despite low temperature ($< 0^\circ C$). The presence of "ice nuclei" aerosol makes possible the freezing at higher temperature respect to pure water one ($-40^\circ C$). Due to ice nuclei scarcity, freezing process becomes efficient at about $-15^\circ C$.

At the same time the phase transition also takes place through the sublimation of vapor on ice nuclei.

Liquid and frozen hydrometeors grow through diffusion, collision and coalescence processes. The diffusional process is more relevant in ice crystals growth, while the collision and coalescence process prevails in liquid droplets. This second process prevails in sufficiently large drop sizes.

At mid-latitudes, the presence of ice particles that grows by diffusion and melts during the fall is important for precipitation occurrence.

A cloud is composed by several hundreds of droplets per cubic centimeter with radii of about 10 μm (Rogers and Yau, 1989); typical droplet and drop sizes are shown in Fig. 1.1. When clouds also contain ice crystals, these particles have similar diameters but a density of some order lower than droplets.

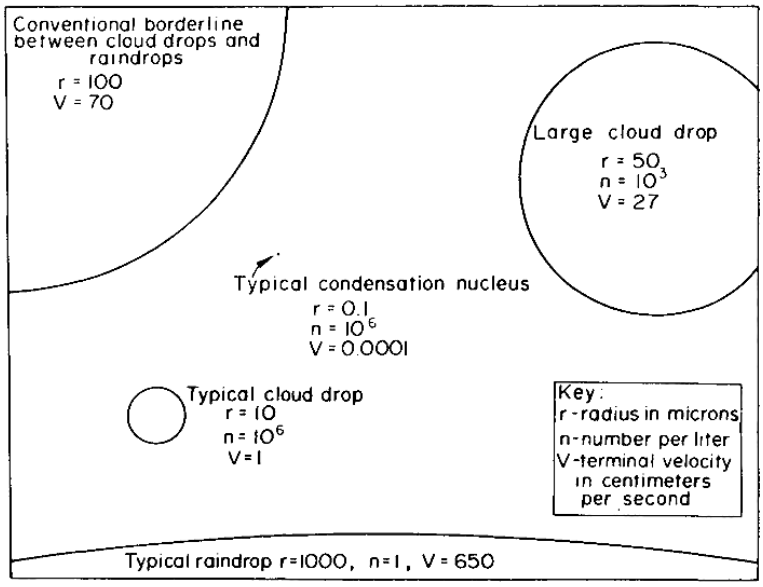

Figure 1.1: Comparison in radius r, concentration n and fall velocity V of droplets in the atmosphere. Source: McDonald, 1958.

When a drop reaches a radius of 0.1 mm it begins to fall and during the descent it may evaporate or grow; a typical rain drop has a radius of 1 mm. On average in case of precipitation, 1m^3 of air contains about 10^3 raindrops (Uijlenhoet and Sempere Torres, 2006), frozen hydrometeors are usually sparser.

Falling particles have terminal velocities w_t, i.e. the maximum vertical velocity of a particle in the air, that depend on their sizes. Atlas and Ulbrich (1977) propose a relation between terminal velocity w_t (ms^{-1}) and size D (mm):

$$w_t(D) \simeq 3.78 D^{0.67}. \tag{1.1}$$

In presence of frozen particles again relationships between velocity and diameters exist. For hailstones, the experimental result by Matson and Huggins (1980) is reported:

$$w_t(D) = 3.62 D^{1/2}. \tag{1.2}$$

For snowflakes, Gunn and Marshall (1958) find that

$$w_t(D) = 0.98 D^{0.31}. \tag{1.3}$$

Substituting typical diameter values in Eqs. 1.1, 1.2, 1.3, the usual velocity values are ranged between [1-10] ms^{-1} for liquid drops, [8-20] ms^{-1} for hailstones and [0.5-2] ms^{-1} for snow. However, frozen hydrometeor relations are highly dependent on factors such as the particle density and shape, so velocities can be remarkably different from the predicted ones.

1.1.1 Precipitating hydrometeor types

Precipitating hydrometeors are divided in liquid and frozen phases. Liquid particles are classified as drizzle when appear almost to float and usually have a diameter of less than 0.5 mm, while they are classified as rain when have sizes ranging from 0.5 mm to few millimeters. Depending on their size, rain drops can assume various shapes as shown in Fig. 1.2. As described by Doviak and Zrnic (1993), drops of diameter D smaller than 0.35 mm are essentially spherical, up to 1 mm they have an oblate shape; for bigger dimensions drops tend to flatten and then to have a concave base.

Figure 1.2: Typical shapes of falling drops. From left to right, the diameters D are: 8.00, 7.35, 5.80, 5.30, 3.45, and 2.70 mm. Source: Puppacher and Beard, 1970.

Frozen particles are classified into graupel, hail, ice crystal and snow. Graupel is composed by a central ice nucleus covered with frozen cloud droplets that forms when a particle of ice, usually a crystal, collects supercooled cloud droplets which rapidly freeze ("riming" process). It is generally conical or rounded, opaque with density varying from 0.05 g cm^{-3} to as high as 0.89 g cm^{-3} and its diameter ranges between 0.5 mm and 5 mm (Pruppacher and Klett, 1997). Hail has a graupel particle as embryo and it can be formed by various layers that can be transparent or opaque depending on external conditions. Hail occurs with a great variety of forms and dimensions and it reaches diameters up to centimeters with density ranging from 0.5 g cm^{-3} up to approaching that of pure ice of 0.917 g cm^{-3} (List, 1958; Vittori and Di Caporiacco, 1959; Macklin et al., 1960). Precipitating ice crystal and snow, i.e.

an aggregation of ice crystals, have shape and size that vary considerably in function of temperature and supersaturation during their formation. Their dimensions range between 0.2 mm and 0.77 mm (Mitchell et al., 1990).

1.1.2 Convective and stratiform precipitation

Precipitation is commonly classified into two categories: convective and stratiform. Convective precipitation systems are generated by strong vertical velocity fields, with updraft of the order of meters per second. As described by Anagnostou and Kummerow (1997), these systems are typically characterized by very localized precipitation cells with high rainfall intensities. During convective precipitation the presence of graupel and hail may occur. Conversely, stratiform precipitation systems arise from widespread and homogeneous slow ascent velocity fields (few tents of centimeters per second) and produce low intensity and extended rainfall or snowfall.

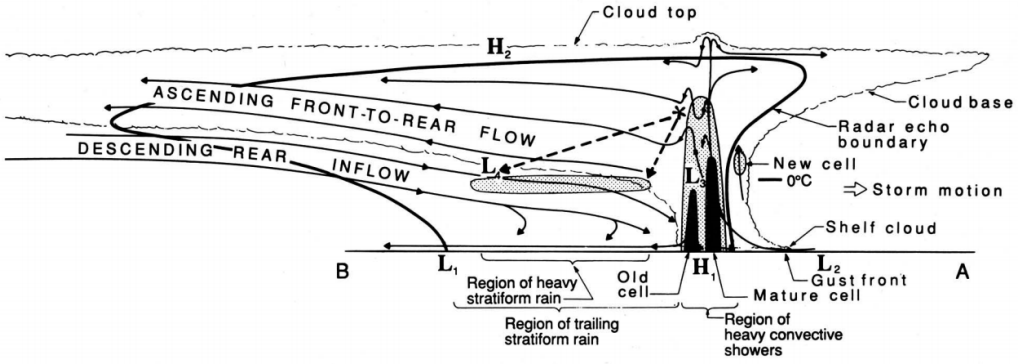

Figure 1.3: Idealized squall-line structure in which both convective and stratiform precipitation regions are identified at the same time. Source: Houze et al., 1989.

Sometimes stratiform and convective precipitation simultaneously occur in the same cloud structure, due to the coexistence of cells at different stages in the life cycle of a storm. Fig. 1.3 shows an example of an idealized "squall line", i.e. an

organized series of thunderstorms.

1.2 Precipitation variables

Precipitation is described through several variables such as duration, cumulative precipitation and rainfall rate. The precipitation duration (min) is defined as the time period in which it rains or snows continuously in a specific area. Since the precipitation is often intermittent it is divided in events. In literature the typical criterion to divide precipitation events is the elapsed time between two precipitation occurrences. Usually, the elapsed time is chosen in the range from 3 minutes to 24 hours (Dunkerley, 2008, 2010).

The cumulative precipitation (mm) is the total amount of precipitation in a specific area during the whole event.

The rainfall rate R measured over a specific area is expressed in terms of length (depth) per unit time; the measurement unit is usually mm h^{-1}.

Cumulative precipitation, rainfall rate and other variables can be retrieved from the Drop Size Distribution (DSD).

1.2.1 Drop Size Distribution

The DSD is "the frequency distribution of drop sizes (diameters, volumes) that is characteristic of a given cloud or a given fall of rain" (AMS glossary).

The *N(D)* (m^{-3} mm^{-1}) is the DSD in which the number of raindrops is considered in function of diameter D per unit volume.

Fig. 1.4 (a) shows qualitative examples of DSD *N(D)*. The red line represents the *N(D)* that is obtained through the physical processes which affect the initial

linear distribution (blue line). The main processes are collision and coalescence, break-up, evaporation. The collision and coalescence of two or more drops cause the decrement of the small particle number and the increment of the number and the size of the larger ones. The larger the size is, more likely the break-up will occur (Komabayasi et al., 1964), causing the larger drops to break into several smaller drops. Since the evaporation is more efficient with smaller particles, it mainly causes the decrease of the smaller particle number and size. As a result, the diameter distributions typically peak at about 1 mm (Rogers and Yau, 1989).

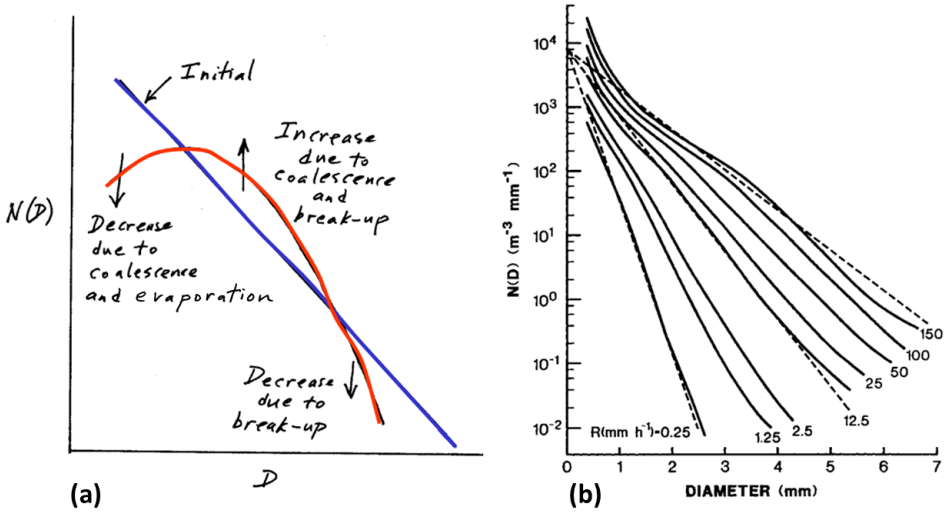

Figure 1.4: Physical processes affecting *N(D)* shape, y-axis is in logarithmic scale (a); *N(D)* measured by Laws and Parsons (solid lines) and fitted with Marshal-Palmer distributions (dashed lines), y-axis is in logarithmic scale (b). Source: edited Rosenfeld and Ulbrich (2003)(a); Doviak and Zrnic (1993) (b).

Figure 1.4 (b) shows the shape of some measured *N(D)* for various rainfall rates (solid lines). All the distributions have a maximum for small diameters and exponentially decay for increasing drop sizes. For higher rainfall a departure from the exponential shape and a local *N(D)* maximum can be detected at about 3-4

mm. Moreover, a decrease of the drop number for $D < 1\,mm$ usually occurs, but it is not observed in the Figure due to the poor resolution of the instruments used for the measurements.

Marshall and Palmer (1948) identify a one-parameter function to reproduce the measured distributions:

$$N(D) = N_0 \exp(-\Lambda D), \tag{1.4}$$

where N_0 is a constant that is equal to 8×10^{-3} m^{-3} mm^{-1} and Λ is the "slope factor" that depends only on the rainfall rate:

$$\Lambda = 4.1 R^{-0.21}\, mm^{-1}. \tag{1.5}$$

In Fig 1.4 (b) the curves retrieved from the Eq. 1.4 (dashed lines) are fitted to the measured distributions. As a result, a good agreement is observed, especially for smaller rainfall rates.

A more complex distribution is introduced by Ulbrich (1983) consisting in a general gamma distribution:

$$N(D) = N_0 D^{\mu} \exp(-\Lambda D), \tag{1.6}$$

where μ is the second adimensional parameter that usually assumes values between -3 and 8 (Doviak and Zrnic, 1993).

For precipitation characterized by snowflakes, Gunn and Marshall (1958) realized that the Eq. 1.4 is still a good representation, with N_0 and Λ equal to

$$N_0 = 3.8 \times 10^3 R^{-0.87}, \tag{1.7}$$

$$\Lambda = 2.55 R^{-0.48}\, mm^{-1}. \tag{1.8}$$

Regarding hailstone precipitation, among the several studies carried out, Cheng and English (1983) work is introduced for the reason of its simplicity (Doviak and Zrnic, 1993). Seven thunderstorms in Alberta (Canada) are analyzed, resulting in a single parameter Λ distribution that has the form of Eq. 1.4 with

$$N_0 = 115\Lambda^{3.63}. \tag{1.9}$$

Several precipitation parameters are derived as moments of the *N(D)*. For example, knowing the *N(D)*, the rainfall rate can be retrieved by the 3.67^{th} moment of the distribution:

$$R = 6\pi 10^{-4} \int_0^\infty D^3 N(D) w_t(D) dD. \tag{1.10}$$

1.2.2 Reflectivity factor

The reflectivity factor Z ($mm^6 m^{-3}$) is now introduced. Z is a very important radar variable and it can be defined as the sixth moment of the distribution:

$$Z = \sum_V D^6 = \int_0^\infty N(D) D^6 dD. \tag{1.11}$$

For raindrops, $N(D)$ is the size distribution of the drops. For ice-phase, $N(D)$ is the distribution of the drops obtained after the fusion of the ice particles.

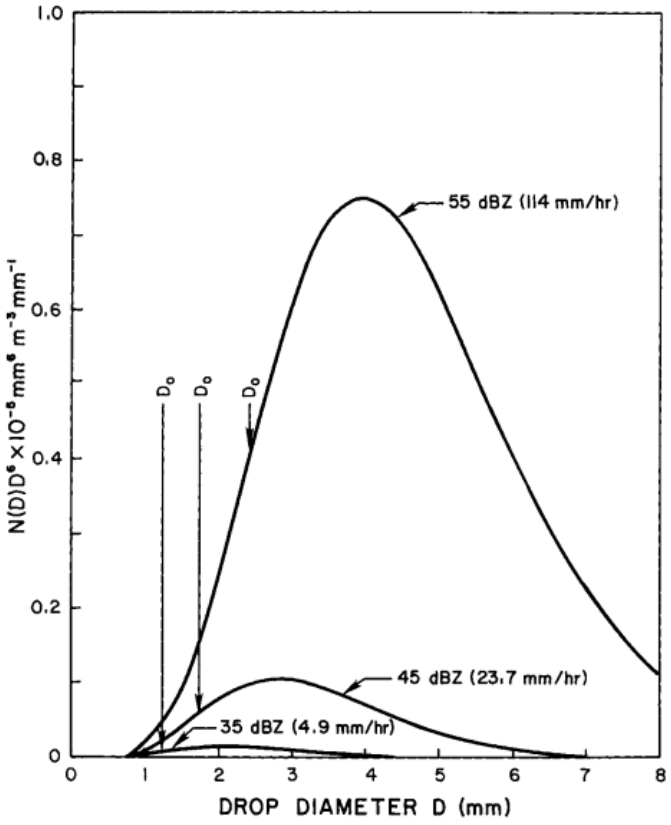

Figure 1.5: Reflectivity factor integrand $N(D)D^6$; D_0 is the median volume diameter of the drops. Source: Doviak and Zrnic (1993).

Since the reflectivity factor ranges over a wide span of order of magnitudes, it is often expressed in "dBZ" units. The reflectivity factor in dBZ ζ is defined as

$$\zeta = 10 \log_{10} \left(\frac{Z}{Z_1} \right), \tag{1.12}$$

where Z_1 is the reference value of 1 mm^6 m^{-3}. From here on ζ is replaced by Z.

Fig. 1.5 shows the integrand of Eq. 1.11 for three different rainfall intensities, using the Marshall-Palmer distribution (Eq. 1.4). Although the distributions are dominated by small drops (Fig. 1.4 (b)), considering the dependence of Z to the

sixth power of the diameter, the main contribution is given by the large drops. An advantage of using the reflectivity factor is that the poor quality representation of small drops by Eq. 1.4 does not lead to big errors.

1.3 Measuring the precipitation

The aim of this section is to summarize the instruments used for precipitation measurement. These measurements are divided in two categories: 1) in situ, when they are taken in the same place the phenomenon is occurring; 2) remotely sensed, when the property of an object or phenomenon are measured by a recording device that is not in physical contact with the object or phenomenon under study (Colwell et al., 1983).

The in situ measurements are performed by rain gauges. Rain gauges are systems designed to measure the amount of precipitation and the rainfall rate. Rain gauges are divided in catching and non-catching. The catching ones include the graduated cylinders, weighing gauges and tipping bucket gauges. The graduated cylinder is simply a graduated bucket, in which the amount of rainfall is estimated by level measurements. The weighing gauge collects and instantaneously measure the amount of precipitation through pressure sensors, frequency measurements or electronic scales. The tipping bucket gauge channels precipitation towards a tilting system usually composed by two bins filled one at a time. The bins have a certain volume so the precipitation parameters are easily retrieved. Non-catching instruments include the disdrometers that allow the measurement of the precipitation structure and they will be introduced in Section 1.5.

Remote sensing measurements are performed by weather radars and satellite

sensors. The firsts are instruments that provide bulk precipitation measurements in their surroundings. They are typically placed at the surface and have measurement ranges in the order of 10^2 km. Weather radars will be widely treated in the next Section. Conversely, satellites orbit around the earth at hundreds of kilometers of altitude. Satellites are equipped with 1) spaceborne radars, which provide three-dimensional maps of storm structure including the rainfall rate at the surface, and 2) passive visible-infrared and microwave imagers that measure the emitted and scattered radiation.

In the next two Sections the instruments used in the present work are described: the weather radar and the disdrometer.

1.4 Weather radar

"The term *radar*, suggested by S. M. Taylor and F. R. Furth of the U. S. Navy, became in November 1940 the official acronym of equipment built for *ra*dio *d*etecting *a*nd *r*anging of objects" (Doviak and Zrnic, 1993). This instrument is a remote sensing tool for the detection of objects characterized by various sizes in the atmosphere through the radio waves. The term *radio* is a generic term applied to all electromagnetic radiation at wavelengths ranging from about 20 km to fractions of a millimeter (Doviak and Zrnic, 1993).

Weather radars work in the microwave electromagnetic spectrum, defined by spatial wavelengths ranging between 10^{-3} m and 10^{-1} m. The band designation of the microwave spectrum is represented in Tab. 1.1.

Band name	Frequency
HF	3 - 30 MHz
VHF	30 - 300 MHz
UHF	300 - 1000 MHz
L	1 - 2 GHz
S	2 - 4 GHz
C	4 - 8 GHz
X	8 - 12 GHz
Ku	12 - 18 GHz
K	18 - 27 GHz
Ka	27 - 40 GHz
V	40 - 75 GHz
W	75 - 110 GHz
mm	110 - 300 GHz

Table 1.1: Band designation of the microwave spectrum according to radar-frequency band nomenclature (IEEE Std. 521-2002).

The weather radar offers many meteorological applications such as:

- the possibility to retrieve information through optically opaque areas such as clouds and precipitation systems;
- the detection of a precipitation-system evolution;
- the possibility to retrieve information during the nighttime, because the radar measurements do not depend on sun radiation;
- the sampling in three dimensions acquiring volumes without modifying the targets.

Typically in weather radar bands S, C and X are used:

- S-band radar is principally deployed in areas where extreme precipitation events, such as large hail and heavy rain, are not rare: NEXRAD in the United States of America is the largest S-band network with 160 radars.
- C-band radar is used where heavy rain and hail are less frequent. This is the type of radar used in this work.
- X-band radar is mainly adopted in shorter-range hydrological and meteorological applications.

The World Meteorological Organization (WMO) weather radar database contains metadata for 835 of the estimated 1500 operational weather radars in the world. Of these, approximately 40% (335) are S-band and 53% (446) are C-band[1].

1.4.1 Radar operating principles

A schematized radar structure is resumed in three principal components: transmitter, antenna and receiver.

The transmitter creates electromagnetic pulses or continuous waves characterized by high power in the radio-frequency portion of the spectrum. Most radars, included the one used in the present Thesis, emit pulsed waves and are called "pulsed radars". As shown in Fig. 1.6 a pulse has a duration τ, a base frequency f_0 and a pulse repetition time (PRT) T_c, i.e. the elapsed time between two successive pulses. Inverting T_c the pulse repetition frequency (PRF) is obtained, which is the number

[1] https://public.wmo.int/en/resources/meteoworld/meteorological-radar-world-radiocommunication-conference

of radar pulses per second. The product of τ and PRF is called the "duty cycle" of a radar system, i.e. the fraction of time during which the system is transmitting.

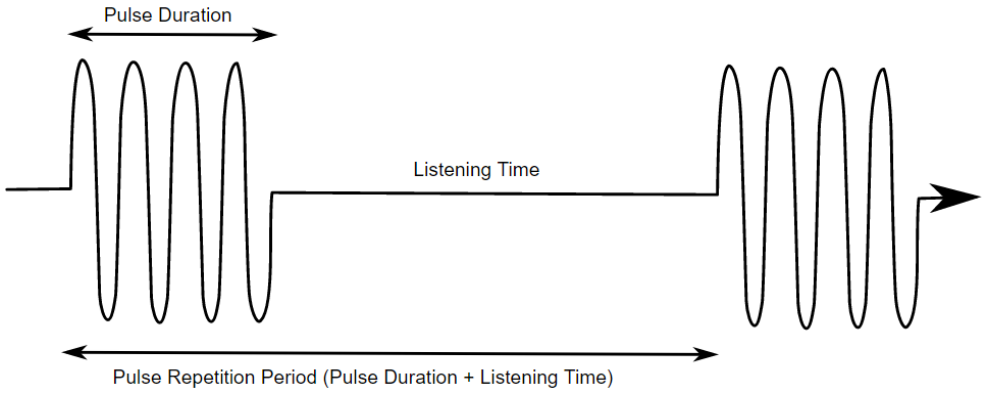

Figure 1.6: Schematized electromagnetic pulses emitted by the radar. Source: echopedia.org.

These pulses are focused in a narrow beam by the antenna, that propagates at the light speed c. The beam interacts with a volume of matter, mainly with objects present in the atmosphere causing the absorption and the redistribution of the energy in all directions. Part of the scattered energy propagates back to the antenna (*backscattering*) and if this component is large enough, it is revealed by the receiver and visualized through the display. In Subsection 1.4.5, the scattering processes are described in more detail.

The distance of the target d is revealed through the simple calculation $d = cT/2$, where c is the speed of light in vacuum and T is the elapsed time between the transmission and the reception of the beam. Using the speed of light in vacuum instead of the one in the air does not cause in first approximation a significant error in the distance computation.

Sometimes radars have two antennas (bistatics), one for transmitting and one for receiving purpose. Operational weather radars normally have only one antenna

(monostatics) for transmitting and receiving the signal.

A characteristic of many radars is the coherence, which means that the phase of the transmitted beam is known. This property allows to use the Doppler effect and in this case radars are named "Doppler radars". These radars can measure the radial speed of the particles.

Modern radars, included the one of this work, can afford polarization measurements. This property allows the measurement of several hydrometeors characteristics such as size, shape, spatial orientation and thermodynamic phase (Doviak and Zrnic, 1993). These types of radar are defined "polarimetric radar", whose properties are underlined in Subsection 1.4.6.

1.4.2 Antenna beam

The outgoing beam begins to spread, cause of diffraction, into a conical having an angular width given by

$$\Delta\vartheta \simeq 104\lambda/D, \tag{1.13}$$

expressed in degrees, where D is the diameter of the antenna system and λ the wavelength of the beam.

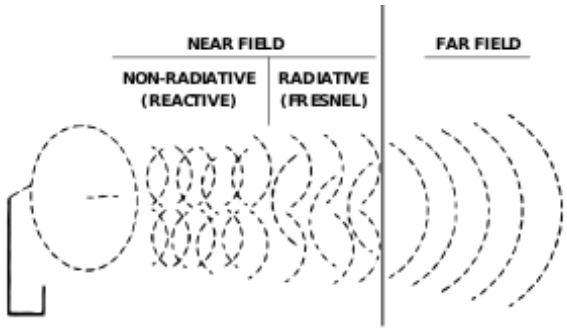

Figure 1.7: Radiation patterns exiting from the antenna. Source: wikimedia.org.

The atmosphere is uniformly irradiated at a distance of $2D^2/\lambda$, beyond which the far-field region ("Fraunhofer region") starts. The diffusion of the radiation beam is schematized in Fig. 1.7, where it is distinguished the uniform far field region. Only in that region the signal analysis have enough quality.

The geometrical characteristics of the antenna affect the beamwidth and the antenna gain. The beamwidth β_{-3dB} is defined as the aperture in which the magnitude of the radiation pattern decreases by a half power (-3dB). Considering the main lobe of the antenna beam as gaussian, β_{-3dB} is defined as

$$\beta_{-3dB} \simeq 70\,\lambda/D, \tag{1.14}$$

expressed in degrees. The smaller the beamwidth is, the larger the data resolution will be improving the detection in the far regions from the radar. The antenna gain $G(\theta, \phi)$ expresses the ability to concentrate energy in a specific direction, also taking into account the antenna losses η_l. In a simple form, the antenna gain is defined as

$$G(\theta, \phi) = \eta_l D(\theta, \phi), \tag{1.15}$$

where the coefficient η_l typically varies between 0.5 and 0.7 and $D(\theta, \phi)$ is the directivity, i.e. the ratio between the radiation intensity in a given direction from the antenna and the radiation intensity averaged over all directions.

1.4.3 Beam propagation

In a homogeneous mean the beam waves propagate in straight lines because the dielectric permittivity ϵ and the magnetic permeability μ are constant, so the speed

of light $v = 1/\sqrt{\mu\epsilon}$ is constant too. The earth atmosphere is vertically stratified, causing the deflection of the transmitted beam by the radar according to Snell's law.

Since the refractive index n is defined as $n = c/v$, the computation of n allows to study the shape of the beam propagation path.

The refractive index is proportional to the density of the molecules and their polarization, in fact it depends on temperature, pressure and water vapor content of the air. Despite it varies little in atmosphere, a change to the sixth decimal may bring to a significant modification of the wave propagation path.

Since the variability of n is low at microwave frequencies, the refractivity N is introduced:

$$N = (n - 1) \times 10^6. \tag{1.16}$$

N can be obtained from the following formula:

$$N = (77.6/T)(P + 4810P_w/T), \tag{1.17}$$

where T is the temperature (K), P and P_w are respectively the total and the partial pressure of water vapor (hPa). The Eq. 1.17 points out that N is more suitable than n, because it may be determined at any height measuring T, P and P_w. In the troposphere, both temperature and pressure usually decrease increasing the height. Typically the decrease in pressure is larger than the decrease in temperature, so N diminishes with altitude.

The horizontal homogeneity of the refractive index is a reasonable approximation for most applications. This approximation allows to consider the refractive index only a function of height. As reported by Doviak and Zrnic (1993), the great circle distance s (m) along the Earth surface to a point below the ray at height h

above the surface is expressed as

$$s(h) = \int_0^h \frac{aC\,dh}{R\left[R^2 n^2(h) - C^2\right]^{1/2}}, \tag{1.18}$$

where a is the earth radius and $C = an(0)\cos(\theta_e)$ in which $n(0)$ and θ_e are respectively the refractive index and the elevation angle at the transmitter location. $n(h)$ is assumed to vary smoothly, so the ray theory is exploited.

For considering the beam deflection due to the air stratification, the effective earth's radius model is introduced. As highlighted by Fig. 1.8, the curvature C_0 of any line is given by

$$C_0 = \frac{\left[R^2 + 2\left(\frac{dR}{d\psi}\right)^2 - R\frac{d^2R}{d\psi^2}\right]}{\left[R^2 + \left(\frac{dR}{d\psi}\right)^2\right]^{3/2}}, \tag{1.19}$$

where $R = a + h$ and ψ is the zenith angle. Since in the lower atmosphere $h \ll a$, replacing R by a and dR by dh are good approximations and Eq. 1.19 becomes

$$C_0 \simeq \frac{1 + 2\left(\frac{dh}{ds}\right)^2 - a\frac{d^2h}{ds^2}}{a\left[1 + \left(\frac{dh}{ds}\right)^2\right]^{3/2}}, \tag{1.20}$$

in which $s = a\psi$ is considered because ψ is small enough for assuming $\sin(\psi) \simeq \psi$. In the examined conditions, noting that $n \simeq 1$ and $(dh/ds) \ll 1$ the curvature formula results:

$$C_0 \simeq -\frac{dn}{dh}. \tag{1.21}$$

Hence C_0 is a function of the vertical gradient of n. The variation of n in the first 1-2 km of a real atmosphere is well approximated by a linear function so the curvature of the beam is constant.

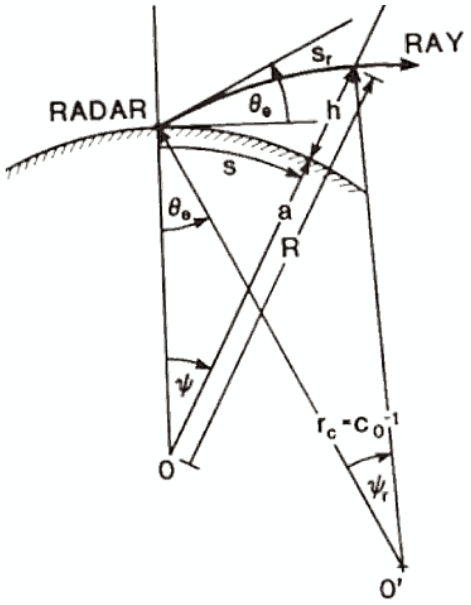

Figure 1.8: Beam path in an n vertically stratified atmosphere. Source: Doviak and Zrnic, 1993.

An equivalent homogeneous atmosphere where the beam paths are straight is considered. Fixed the arc distance s, the "new" earth radius a_e is computed such that the height of the straight beam is the same of the actual height h. After some calculations it is obtained that if the linear approximation of n is valid, then the earth radius is equal to

$$a_e = \frac{a}{1 + a\left(\frac{dn}{dh}\right)} = k_e a, \tag{1.22}$$

where k_e is therefore a constant. The result is the formulation of h and s related to measurable radar variables range r, defined as d in the previous Subsection, and ϑ_e:

$$h = \left[r^2 + (k_e a)^2 + 2 r k_e a \sin\theta_e\right]^{1/2} - k_e a, \tag{1.23}$$

$$s = k_e a \sin^{-1}\left(\frac{r\cos\theta_e}{k_e a + h}\right). \tag{1.24}$$

It has been found empirically that the value of the gradient of the refractive index in the first kilometers is ordinarily $-1/4a$, so

$$k_e = 4/3. \tag{1.25}$$

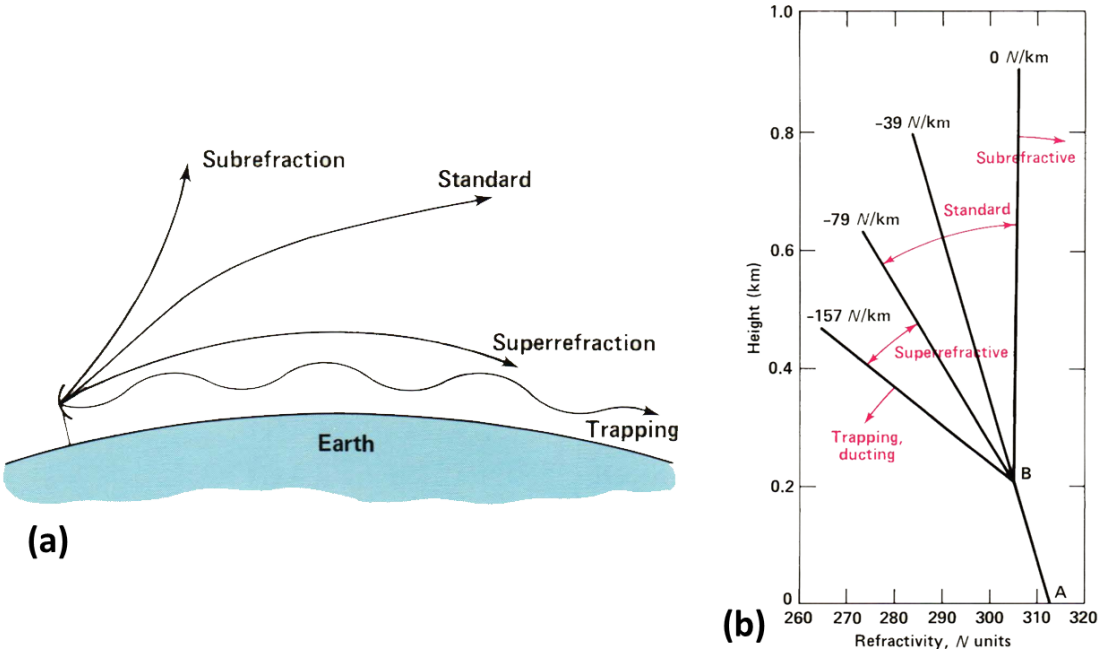

Figure 1.9: Types of anomalous propagation of the radar beam (a); ranges of refractivity profile slopes N/km for type of propagation (b). Source: Harvey et al., 1983.

Departures from the effective earth's radius model occur when the propagation is "anomalous" and the gradient dn/dh may not be approximated as linear. In the atmosphere the anomalous propagation occurs in terms of subrefraction, superrefraction and trapping. Compared to normal propagation paths, subrefraction is the bending up of beams, superrefraction is the bending down of beams and trapping is the strong bending down of beams. These types of anomalous propagation are depicted in Fig. 1.9 (a). The height gradient of refractivity allows to understand

which type of anomalous propagation is likely to occur. Figure 1.9 (b) reports the intervals of refractivity gradient within the different types of propagation occur.

Bending down of the beam is typically in case of temperature inversions. The example shown by Doviak and Zrnic (1993) is reported. In this example the atmosphere has a refractivity gradient of $-300\,km^{-1}$ in the first 100 meters and a gradient associated with the effective earth's radius model above. Resulting beam paths for some radar elevation angles are shown in Figure 1.10. For small angles (i.e. $\leq 0.2°$) the beam is trapped by the ground within 50 km, while for larger elevation angles the bending is less evident. As consequence, a broadening of the detected volume also occurs, causing the lowering of the resolution.

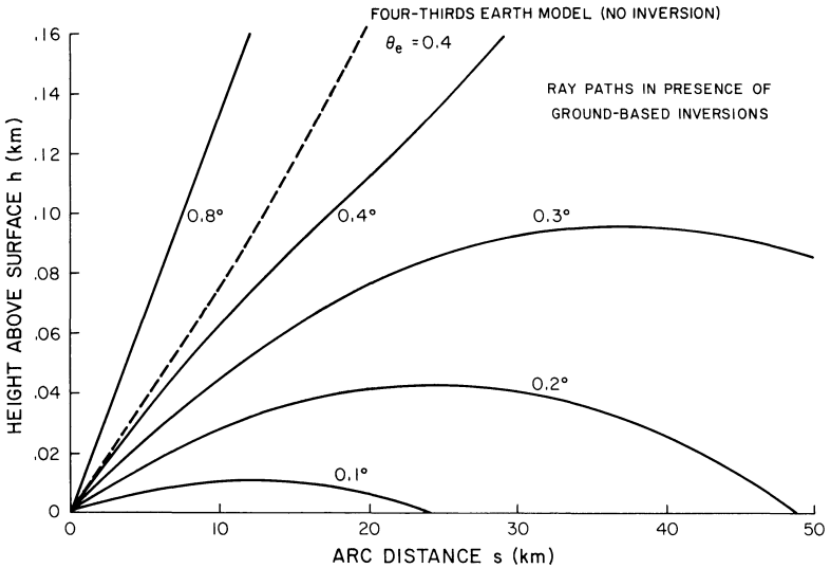

Figure 1.10: Beam paths in an atmosphere in which a severe gradient of refractivity in the first 100 meters occurs. Dashed line represents the path in the effective earth's radius model. Source: Doviak and Zrnic, 1993.

Babin (1996), Alberoni et al. (2001) and Bech et al. (2002) observe that the highest incidence of superrefraction is in summer and during the night. Conversely, subrefraction may occur when high humidity is present up to high altitudes, for

example in rain conditions. Moreover, subrefraction is more likely when humid and cooler air is below dry and warm air.

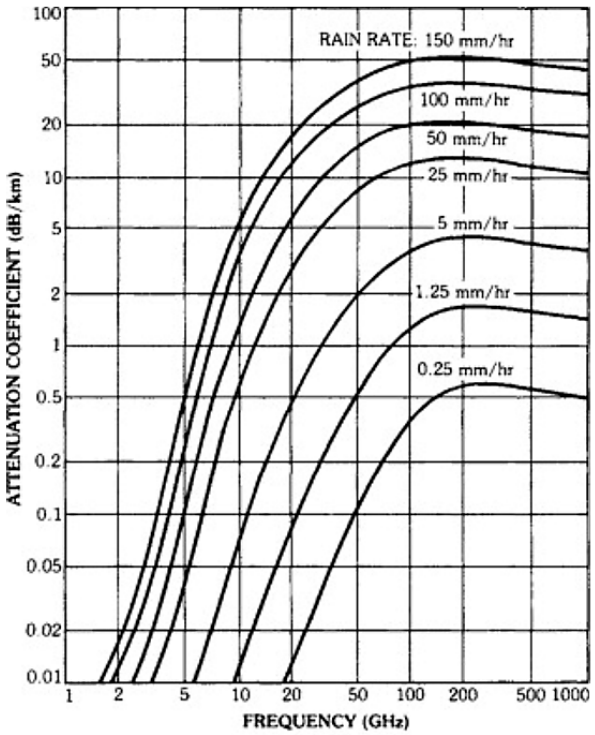

Figure 1.11: Attenuation (dB) per km versus the frequency of the beam and the rain rate (Evans, 1983).

Another condition affecting the beam propagation is the attenuation due to the atmosphere. The beam attenuation is negligible at frequencies below about 10 GHz in case of clear air (Rinehart, 1991). The attenuation is no longer small in case of cloud or rain conditions, especially during heavy rainfall (see Fig. 1.11). Contrariwise, the attenuation is negligible in case of snowfall unless the snow is melting.

1.4.4 Radar range limitations

The weather radar has different measurable range depending on its characteristics.

If the radar is monostatic, it cannot receive during the transmitting time because the receiver is switched off. Therefore, a minimal measuring range R_{min} ("blind range") exists. R_{min} is the minimum distance from the antenna that an object must have to be detected. This distance is determined by 1) the time taken by the transmitting pulse to completely leave the antenna and 2) the recovery time $T_{recovery}$, which is the time needed by the radar unit to switch on the receiver. R_{min} is expressed as

$$R_{min} = \frac{c \cdot (\tau + T_{recovery})}{2}. \tag{1.26}$$

Conversely, the maximum range R_{max} is defined as the range to which a transmitted pulse can travel and return before the next pulse is transmitted. R_{max} is expressed as:

$$R_{max} \simeq \frac{c}{2\,PRF}. \tag{1.27}$$

Therefore, the maximum range is set by the choice of the PRF value. Radar echoes of precipitation systems located further away than R_{max} are defined "second trip echoes". The radar is not able to properly detect these echoes. As a consequence, they appear at incorrect ranges, elongated and with weaker signal. This issue is resolved using staggered PRFs during consecutive radar acquisitions.

1.4.5 Weather radar equation

Meteorological particles as rain, snow or hail are distributed targets in the atmosphere. The radar beam illuminate simultaneously all the targets located in a given

volume. This volume is named "resolution volume" V and it is determined by the pulse length and the beam width. For a circular beam, V can be defined as

$$V = \pi \left(\frac{r\beta_{-3dB}}{2} \right)^2 \frac{h}{2}, \tag{1.28}$$

where r is the distance of the targets and $h = c\tau$ is the pulse width in terms of length.

For distributed targets, particles move relative to each other, so the power returned from a given resolution volume is observed fluctuating over time. These relative motions are caused by the wind and the presence of hydrometeors of different size, shape and type, which have different fall velocities. A sufficient long time average ($\simeq 10^{-2}\, s$) of the power received by the antenna $\overline{P_r}$ can be expressed as

$$\overline{P_r} = P_t \frac{G^2 \lambda^2}{(4\pi)^3 r^4} \sum \sigma, \tag{1.29}$$

where P_t is the peak power, G is the gain defined in Eq. 1.15, λ is the wavelength of the beam and σ the backscattering cross section, that regulates the portion of incident wave energy that is scattered from the object back in the direction of the incident wave. As a consequence, $\sum \sigma$ is the sum of the backscattering cross sections of all the particles into the resolution volume. In the scattering process the oscillating electric field of the radar beam acts on the charges within a target, causing them to move at the same frequency. Therefore, each target becomes a radiating dipole that emits electromagnetic waves in all directions.

The scattering processes are analyzed through the Mie theory, that represents a generalized solution to Maxwell's equations. This solution describes the scattering

of an electromagnetic plane wave by a homogeneous sphere, where the size of the scattering sphere is comparable to the wavelength of the radar beam. This theory is based on a dimensionless shape parameter a defined as :

$$\alpha = 2\pi r_0/\lambda, \tag{1.30}$$

where r_0 is the radius of the scattering sphere. For a single spherical scatterer that is small compared to the radar wavelength (for small α), the formulation of Mie backscattering cross section (here not shown) reduces to:

$$\sigma = 64\frac{\pi^5}{\lambda^4}\left|K\right|^2 r_0^6, \tag{1.31}$$

where $K = (m^2–1)/(m^2+2)$ is a dielectric factor with $m = n–ik$ complex refractive index of the sphere; n is the real part of the refractive index and k the absorption coefficient. This formulation derives from the Rayleigh law and particles small enough for which it applies are called Rayleigh scatterers. Considering the typical radar wavelengths S, C and X, liquid droplets can be considered good Rayleigh scatterers, while for large hail the approximation is less accurate due to the hail size. The refraction term K in Eq. 1.31 depends on temperature, wavelength and phase of the spheres. For wavelengths used in weather radars and over the entire range of temperatures of meteorological interest $|K|^2 \simeq 0.93$ for water and 0.21 for ice. As a consequence, a liquid and a frozen sphere of the same size have different backscattering cross sections. In case of melting snow or hail the σ assumes big values. These large values occur in an atmospheric region defined as “bright band” (or melting layer). This peak is also caused by less density and smaller size of drops

under this layer (Rinehart, 1991).

In terms of Z (Eq. 1.11), substituting the Eq. 1.31 in Eq. 1.29 the radar equation also including a small correction for the gaussian pattern of the beam is defined in its most common form (Rogers and Yau, 1989):

$$P_r = \frac{\pi^3 c}{1024 \ln 2} \underbrace{\left[\frac{P_t \tau G^2 \beta^2_{-3dB}}{\lambda^2} \right]}_{Radar} \underbrace{\left[l^2 \left| K \right|^2 \frac{Z}{r^2} \right]}_{Target}, \tag{1.32}$$

where $l(r)^2$ represents the power losses in the atmosphere. This is the most useful form of the radar equation, because radar and target parameters are written separately. As described by Crozier (1986) this equation is valid under a sum of assumptions. Main hypothesis are that the drops which comprise the target are evenly distributed throughout the sampling volume and of the same type. The measured power P_r is assumed to be averaged on a sufficient number of independent pulses or independent samples, such that P_r is representative of the analyzed volume. Another hypothesis is that all the power losses in the waveguide and in the atmosphere are considered. Aforementioned approximations are always considered, so spherical scatterers are small compared to the radar wavelength (condition for Eq. 1.31) and the beam pattern is gaussian. These assumption are quite accurate for stratiform precipitation, less accurate for convective precipitation.

The radar reflectivity factor Z measured by the instrument and retrieved by Eq.1.32 can be expressed as reported by Rinehart (1991):

$$Z = P_r C r^2, \tag{1.33}$$

where C is a radar constant.

When the assumption for Eq. 1.32 fails, a slightly different quantity should be introduced in place of Z. This quantity is called "equivalent" (or "effective") radar reflectivity factor Z_e, which is the reflectivity of a spherical liquid hydrometeor satisfying Rayleigh approximation and backscattering a signal of the same power as that which is effectively backscattered.

1.4.6 Polarimetry

As mentioned in Subsection 1.4.1 modern radars often allow polarimetric measurements. Polarimetric radars transmit and receive pulses with a specific horizontal H or vertical V polarization depending on the planes of symmetry of the antenna lobe.

Since the radar is able to receive the two linear polarizations H and V, the backscattering matrix [**S**] that relates backscattered electric field $[\mathbf{E}]^b$ at the antenna to the incident electric field $[\mathbf{E}]^i$ at the target, is introduced. The equation describing this relation is (Doviak and Zrnic, 1993):

$$\begin{bmatrix} E_h \\ E_v \end{bmatrix}^b = \begin{bmatrix} s_{hh} & s_{hv} \\ s_{vh} & s_{vv} \end{bmatrix} \begin{bmatrix} E_h \\ E_v \end{bmatrix}^i \frac{\exp(-jkr)}{r}. \tag{1.34}$$

In [**S**] all the terms have two indices: the first refers to the received polarization, the seconds to the transmitted one; "h" and "v" represent horizontal and vertical polarization, respectively. The diagonal terms s_{hh} and s_{vv} are called "co-polar", because transmitted and received polarization have the same orientation, meanwhile s_{hv} and s_{vh} are named "cross-polar" because the power is received at the orthogonal polarization compared to the transmitted one.

Weather radars measure and process the signal voltages instead of the electric

field to retrieve the characteristics of the hydrometeors. The signal voltage is the result of the summation over each individual scatterer and its mean value is zero, thus second-order moments of the voltage are commonly used. These moments are related to properties of the hydrometeors and are multiples of the time-averaged Backscattering polarization Covariance Matrix BCM, defined as

$$BCM = \begin{pmatrix} \left\langle |s_{hh}|^2 \right\rangle & \langle s_{hv} s_{hh}^* \rangle & \langle s_{vv} s_{hh}^* \rangle \\ \langle s_{hh} s_{hv}^* \rangle & \left\langle |s_{hv}|^2 \right\rangle & \langle s_{vv} s_{hv}^* \rangle \\ \langle s_{hh} s_{vv}^* \rangle & \langle s_{hv} s_{vv}^* \rangle & \left\langle |s_{vv}|^2 \right\rangle \end{pmatrix}, \tag{1.35}$$

where the brackets $< >$ represent the expected values for statistically distributed particles. Some retrieved quantities from the BCM are:

1. Horizontal reflectivity factor

$$Z_h = (4\lambda^4/\pi^4 \left|K_w\right|^2) \left\langle |s_{hh}|^2 \right\rangle, \tag{1.36}$$

2. Vertical reflectivity factor

$$Z_v = (4\lambda^4/\pi^4 \left|K_w\right|^2) \left\langle |s_{vv}|^2 \right\rangle, \tag{1.37}$$

3. Differential reflectivity

$$Z_{DR} = 10 \log \frac{\left\langle |s_{hh}|^2 \right\rangle}{\left\langle |s_{vv}|^2 \right\rangle}, \tag{1.38}$$

4. Linear depolarization ratio

$$LDR_{vh} = 10 \log \frac{\left\langle |s_{hv}|^2 \right\rangle}{\left\langle |s_{hh}|^2 \right\rangle} \tag{1.39}$$

or

$$LDR_{hv} = 10 \log \frac{\left\langle |s_{vh}|^2 \right\rangle}{\left\langle |s_{vv}|^2 \right\rangle}, \tag{1.40}$$

5. Correlation coefficient

$$\rho_{hv} = \frac{\left\langle s_{hh} s_{vv}^* \right\rangle}{\left\langle |s_{hh}|^2 \right\rangle^{1/2} \left\langle |s_{vv}|^2 \right\rangle^{1/2}}. \tag{1.41}$$

Z_h and Z_v are respectively the horizontal and the vertical component of the reflectivity factor Z.

Z_{DR} (dB) represents the ratio between the returned horizontal and vertical power. This parameter depends on the asymmetry of the particle shape. The shape is defined through x and y, i.e. the horizontal and vertical axes. Large drops are characterized by $Z_{DR} > 0$ because they usually have oblate shapes ($x > y$, see Fig. 1.2), while small drops are spherical so Z_{DR} values are close to zero ($x \simeq y$); prolate particles have $Z_{DR} < 0$ ($x < y$). Graupel, hail and aggregates of ice crystal tend to roll as they fall, assuming random orientations and as consequence $Z_{DR} \sim 0$. The range of Z_{DR} is about 0-4 dB at S-band, while Z_{DR} may assume larger values at C-band because of resonance (Zrnic et al, 2000). When the radar has an unique receiver, Z_{DR} is insensitive to radar hardware calibration, but it is extremely sensitive to differential attenuation.

LDR_{vh} (dB) is the ratio between the vertical power return from a horizontal pulse and the horizontal power return from the vertical pulse, i.e. LDR_{vh} is the ratio between cross-polar and co-polar terms. LDR_{vh} decrease shows the presence of asymmetric particles which major or minor axis is neither aligned nor orthogonal to the electric field. This parameter is a good detector for melting layer and hail.

LDR_{vh} measurement is affected by noise and in case of unique receiver it does not depend on radar calibration and particle density. LDR_{hv} has the same properties of LDR_{vh}, but it is defined with h and v reversed.

ρ_{hv} is the correlation coefficient between the scattering in horizontal and vertical polarization. ρ_{hv} is a measure of the shape variability of the hydrometeors. The correlation is quite perfect ($\rho_{hv} \simeq 1$) for light rain and fixed oriented particles. It decreases for bright bands, hail and mixed precipitation. The vantage of this parameter is that non-meteo signal is clearly distinguishable ($\rho_{hv} < 0.8$). Low correlations means that horizontal and vertical backscatter fields do not vary synchronously.

Other parameters related to polarimetry are introduced. Differential phase Φ_{DP} (°) represents the cumulative differential phase shift between horizontal and vertical polarization and it is defined as

$$\Phi_{DP} = \Phi_{hh} - \Phi_{vv}. \tag{1.42}$$

Anisotropic particles produce different phase shift for the two polarized orientations. For example, the presence of large oblate particles causes a phase difference between the horizontally and vertically polarized wave, so Φ_{DP} increases. This quantity is sensitive to the water or ice content of the target.

Specific differential phase K_{DP} (°km^{-1}) is the range gradient of the Φ_{DP}, expressed as

$$K_{DP} = \frac{1}{2}\frac{\Delta\Phi_{DP}}{\Delta r}, \tag{1.43}$$

where Δr is the range variation. K_{DP} discerns regions where drops are larger and denser, hence where high rainfalls are occurring. K_{DP} is independent of radar calibration in case of radar has an unique receiver. It is unaffected by attenuation

and it is relatively immune to beam blockage, i.e. the obstruction of the radar beam by obstacle such as topography or buildings.

1.5 Disdrometer

The disdrometer is an instrument that measures the drop size distribution of precipitation to get detailed information about the microphysics of the precipitation. Various disdrometer types exist based on different technologies, that allow to measure the size and in some cases the velocity of the hydrometeors. In general, disdrometers measure not only liquid drops, but also frozen hydrometeors. Therefore, the term Particle Size Distribution (PSD) is sometimes used instead of DSD.

As said disdrometers are built through different technologies, employing different physical principles. The Joss-Waldvogel disdrometer (Joss-Waldvogel, 1967) is an electromechanics impact disdrometer, that provides a measure of drop sizes through a vertical force applied by the particles to a transducer causing a pulse during the drop impact (Kinnel, 1976). Another disdrometer type is the Doppler-effect based disdrometer. An example is the Pludix (Prodi et al., 2000) that uses an X-band continuous wave radar signal to detect particles. A third type of disdrometer is the optical disdrometer. This category is divided in Laser-based disdrometers and Two-Dimensional Video Disdrometers (2DVDs). The firsts use the light extinction principle and are described in the next Subsection. 2DVDs are composed by two high speed line scan cameras oriented in order to have size, velocity and shape measurement of the particles.

1.5.1 Laser-based disdrometer

A laser-based disdrometer (Fig. 1.12 (a)) is composed by a laser transmitter and receiver system.

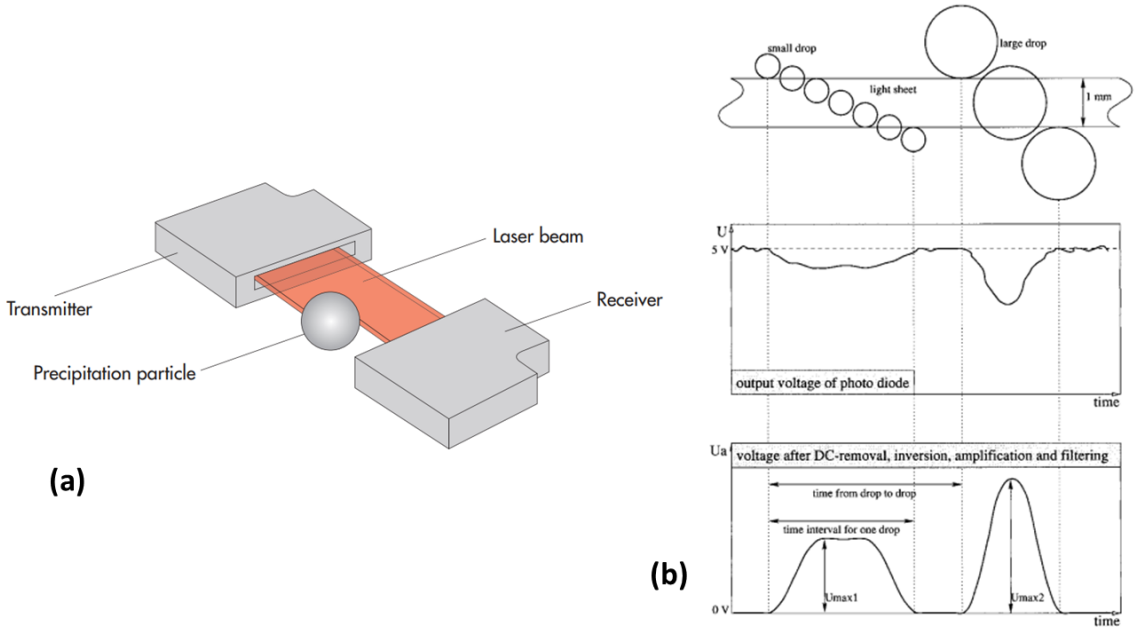

Figure 1.12: Laser- based disdrometer system (a) and measurement process (b); without lack of generality the images refer to PARSIVEL^2 disdrometer (described in details in Chapter 2). Source: OTT, 2016 (a); Löffler-Mang and Joss, 2000 (b).

The term "*laser*" is the acronym for "*l*ight *a*mplification by *s*timulated *e*mission of *r*adiation". It is a device that produces a well coherent and collimated electromagnetic beam by recirculating an internal beam various times through an amplifying medium.

When a hydrometeor passes through the beam, the light intensity is attenuated because of the shadow of the particle. The amplitude and the duration of the beam extinction allow to determine particle size and velocity. Figure 1.12 (b) shows the proportionality of voltage decrease related to the particle size. The signal

is then processed in order to be used.

Chapter 2

Instruments and data

This Chapter describes the characteristics and the datasets of the two instruments used in the present Thesis. In Section 2.1 the characteristics and the sample criteria of the radar and the disdrometer are reported. In Section 2.2 instruments location is shown, underlining the climatology and the morphology of the area. Section 2.3 presents radar and disdrometer datasets and in Section 2.4 the processes of data matching and filtering are outlined.

2.1 Instruments for combined analysis

The instruments used in this study are:

- a C-band polarimetric radar GPM-500C (44.66° N and 11.62° E; Fig. 2.1 (a)) manufactured by ELDES (Italy) and managed by "Struttura Idro-Meteo-Clima" (SIMC) of the "Agenzia regionale per la prevenzione, l'ambiente e l'energia dell'Emilia-Romagna" (ARPAE, Italy);
- a Laser-based disdrometer PARSIVEL^2 (44.50° N and 11.35° E; Fig. 2.1 (b))

manufactured by OTT HydroMet (Germany) and managed by the Physics and Astronomy Department of the University of Bologna (Italy).

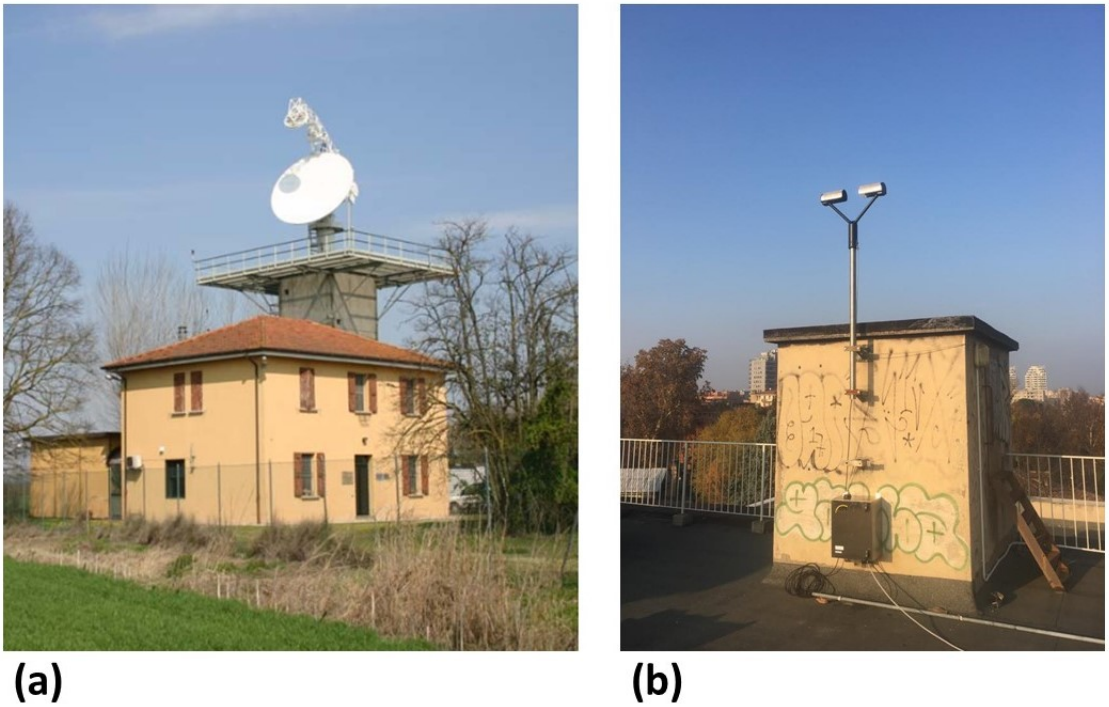

Figure 2.1: Weather radar GPM-500C (a) and disdrometer PARSIVEL^2 (b) used in the present Thesis. Source: SIMC - ARPAE (a); Courtesy of Alessandro Bracci - University of Bologna (b).

2.1.1 Weather radar GPM-500C

The weather radar GPM-500C is a polarimetric Doppler C-band radar. This instrument is equipped with a "magnetron" transmitter. This transmitter is a high-powered vacuum tube that works as a self-excited microwave oscillator, keyed by a modulator which generates a high voltage for the transmitter tube. For construction magnetron is not coherent. Coherence is achieved through a directional coupler that

links the transmitter and the receiver. The phase of the transmitted beam is thus revealed by the receiver and it is compared with the backscattered one. Thus, the radar is defined "pseudo-coherent" or "coherent-on-receive". GPM-500C is monostatic and the type of the antenna-reflector block is a "dual-offset cassegrain" (Fig. 2.2).

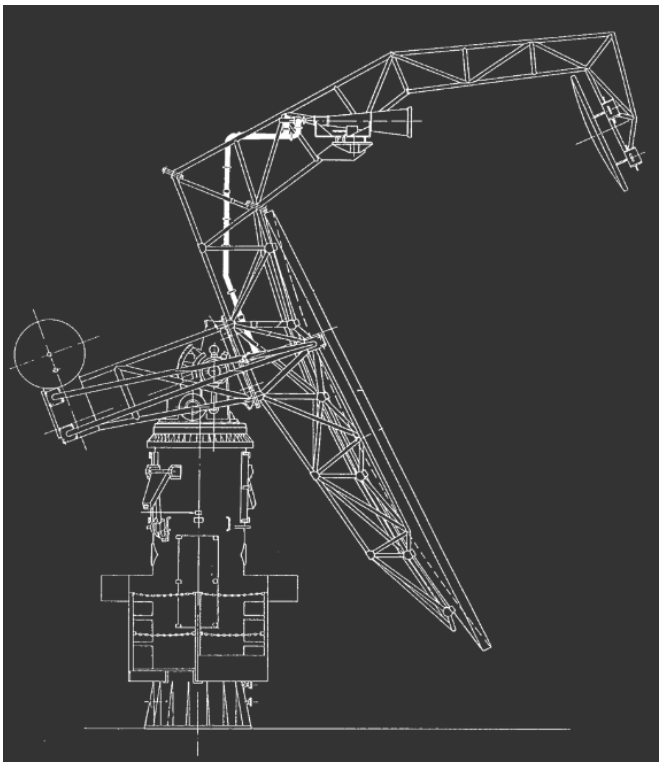

Figure 2.2: GPM-500C dual-offset cassegrain antenna. Edited image from Source: SIMC - ARPAE.

The first part of the antenna-reflector system is composed by a "feed horn" which is basically a horn antenna linked to the transmitter through a waveguide. The horn illuminates the iperbolic dish located in front of it, that in turn irradiates the principal dish, a portion of a paraboloid of revolution. Hence, the beam departs from the principal dish. This peculiar structure aims to keep clean the outgoing

beam from metal components of the antenna.

This radar is equipped with engines that allow the antenna-reflector block to rotate in azimuth and to change the elevation from the ground. Therefore, the radar is able to make different types of acquisition modifying the azimuth or the elevation angle. The acquisition is defined "Plan Position Indicator" (PPI) if the radar collects samples sending pulses at a fixed elevation angle while rotating 360°. This acquisition has the radar located in the center of the displayed data. If the atmosphere is in standard condition, the height of the echoes increases with the distance from the radar and all the points of a certain concentric circumference centered on the radar have the same height. The composition of some PPIs acquired at various elevations, in whose only data at a certain height are held, results in the product defined "Constant Altitude Plan Position Indicator" (CAPPI). The CAPPI gives a horizontal cross-section of data at a constant height. Conversely, a "Range Height Indicator" (RHI) acquisition is made if the azimuth is kept fixed and pulses are sent at various elevations. The RHI provides a vertical cross-section of the atmosphere.

The principal characteristics of the GPM-500C are summarized in Table 2.1.

The radar frequency (5620 MHz) allows to use the Rayleigh approximation up to particles with a diameter of 3.75 mm, equivalent to $\alpha < 0.22$ (Gunn and East, 1954). The Rayleigh approximation for larger diameters is less good, but it is retained with the purpose of continuing to apply the weather radar equation. Diameters larger than the threshold are not uncommon during intense rainfalls (Figure 1.4 (b)).

The radar is employed for weather surveillance by SIMC, making samples every five minutes. The samplings are composed by a cycle of three groups of PPI

acquisitions repeated every fifteen minutes. During the first sampling the transmitted beam has horizontal polarization only, while during the others the polarization is both horizontal and vertical. The properties of the acquisition scans are resumed in Table 2.2. Using the Eq. 1.27, the maximum range is 125 km in the first scan and up to more than 200 km in the other scans.

Characteristics of the GPM-500C radar	
Frequency (MHz)	5620
Peak power (kW)	300
Antenna diameter (m)	5
Beam width	0.9°
Antenna gain (dB)	46
Pulse length (μs)	0.5
PRF	700-2000
Number of integrated pulses	$\simeq 50$

Table 2.1: GPM-500C principal characteristics. The number of pulses (for azimuth angle) typically assumes a value between 40 and 70.

In all scans the radar measures the horizontal radar reflectivity factor Z_h, the radial velocity V_{rad} (ms^{-1}) and the spectral width of the radial velocity W_{rad} (ms^{-1}). Radial velocity and velocity variability are estimated using the Doppler effect. The scans 2 and 3 allow to retrieve polarimetric variables introduced in Subsection 1.4.6. In fact, the radar provides Z_v, Z_{DR}, ρ_{hv} and Φ_{DP}. In addition, the value of the Signal to Noise Ratio (SNR), which is defined as the ratio between the received power and the noise generated by the receiver, is reported. The higher this ratio, the better the sampling.

In the scans 2 and 3 a classification of the prevailing hydrometeor type in the

radar volume is performed, following the algorithm proposed by Park et al. (2009). This hydrometeor classification algorithm is based on the fuzzy logic, which is a logic where the truth value is a number between 0 and 1. Fuzzy is a many-valued logic and it is a sort of extension of the Boolean logic.

Scan number	Start time (min)	Cadence (min)	Elevations	PRF	Polarization
1	00	15	6 (0.5°, 1.4°, 2.3°, 3.2°, 4.15°, 5.0°)	1200	H
2	05	15	11 (0.5°, 1.4°, 2.3°, 3.22°, 4.15°, 5.0°, 7.0°, 9.5°, 13°, 18°, 25°)	700-2000	HV
3	10	15	10 (0.5°, 1.4°, 2.3°, 3.22°, 4.15°, 5.0°, 8.0°, 12°, 18°, 25°)	700-2000	HHV

Table 2.2: Radar PPI acquisitions. In the "Elevations" column, the elevation degrees are specified in brackets. Scan 2 is not achieved in case of fair sky.

For the classification scheme six radar parameters are deployed in input. These parameters are 1) the reflectivity factor Z_h, 2) the linear depolarization ratio Z_{DR}, 3) the cross correlation coefficient ρ_{hv}, 4) the specific differential phase K_{DP} (derived from Φ_{DP}), 5) a texture parameter $SD(Z)$ of the reflectivity factor field and 6) a texture parameter $SD(\Phi_{DP})$ of the field of differential phase Φ_{DP}. $SD(Z)$ and $SD(\Phi_{DP})$ represent respectively the variability of the radar reflectivity and the differential phase along the radial. In addition, the mean Doppler velocity V is used to distinguish between hail and clutter or anomalous propagation. The clutter is an unwanted radar echo generated by ground or obstacles such as buildings. The mean Doppler velocity derives from the time averaging of the radial Doppler velocity v_r:

$$v_r = \frac{\lambda}{2}\Delta\nu, \tag{2.1}$$

where λ is the wavelength of the outgoing beam and $\Delta\nu$ is the frequency shift between the transmitted and the received frequencies.

The hydrometeor class chosen to classify the sample is the one with the highest "aggregation value". This value is a parameter that represents the likelihood that a particular class is associated with the values of variables measured by the radar. The aggregation value A_i for the ith class is defined as

$$A_i = \frac{\sum_{j=1}^{6} W_{ij} Q_j P^{(i)}(V_j)}{\sum_{j=1}^{6} W_{ij} Q_j}, \tag{2.2}$$

where $P^{(i)}(V_j)$ is the "membership function" which is a weighting function that characterizes the distribution of the jth variable for the ith class, W_{ij} is a weight fixed for the ith class and the jth variable, and Q_j is an element of the confidence vector assigned to the jth variable. The confidence vector $\mathbf{Q}$ is related to the quality of the radar measurements, taking in account potential bias and noise. Moreover, the classification is improved adding the information of the hydrometeor position compared to the melting layer. Additional routines as the separation of convective and stratiform echoes are implemented and a set of hard threshold is used to reject clearly wrong classifications.

Hence, the hydrometeor samplings are classified into 1) ground clutter and anomalous propagation (GC/AP), 2) biological scatterers (BS), 3) dry aggregated snow (DS), 4) wet snow (WS), 5) crystals of various orientations (CR), 6) graupel (GR), 7) "big drops" (BD), 8) light and moderate rain (RA), 9) heavy rain (HR) and 10) a mixture of rain and hail (RH). The big drops category designates rain occurrences with a substantial presence of large drops often as a consequence of

strong updrafts or wind changes inside the volume.

2.1.2 Disdrometer PARSIVEL^2

The disdrometer used in the present Thesis is the Laser-based disdrometer PARSIVEL^2, which hides in the name its functionality. In fact, PARSIVEL is the acronym for "PARticle SIze and VELocity", which suggests that this instrument measures the size and the fall velocity of the particles (drops, crystals, hail, ...). PARSIVEL^2 and the previous Parsivel model have a great diffusion because they are easy to handle, robust and low cost; moreover, they allow to detect small drops enabling drizzle measurements (Löffler-Mang and Joss, 2000).

The 5-V strip of light produced by the laser device has dimensions of about 180 mm $\times$ 30 mm and a thickness of 1 mm (OTT, 2016). These dimensions provide a sampling area of 54 cm^2. Then, the calculation of the effective sampling area is performed considering the partially observed hydrometeors (Tokay et al., 2014). The electromagnetic waves that produce the light sheet have a wavelength of 650 nm (OTT, 2016). These waves are received by a photodiode that samples at a frequency of 50 kHz (Park et al., 2017).

The Parsivel measurement process is explained by Löffler-Mang and Joss (2000). As shown in Fig. 1.12 (b), when a particle crosses the laser beam the voltage decreases linearly. The voltage signal is processed through the following steps: the removal of the DC part, inversion, amplification, and filtering. Then an A/D conversion is completed and thresholds are set to reveal the starting time of the particle detection and to measure the maximum attenuation of the signal. The size of the hydrometeors is estimated by the maximum attenuation of the beam and

the fall speed is estimated by the duration of the hydrometeors within the beam (Tokay et al., 2014).

The Parsivel software modifies the shape of the sampled drop according to its size. Defining the equivolume drop diameter as the sphere diameter containing the same volume of water as the drop, if the drop has an equivolume diameter less then a millimeter it is considered spherical. For larger sizes the drop is considered an horizontally oriented oblate spheroid. In particular, the drop axis ratio varies linearly between 1 and 0.7 when the drop size ranges from 1 mm to 5 mm and it is 0.7 for larger drops (Battaglia et al., 2010). In case of snowflakes the particles are assumed as spheres, which sometimes is not a good representation (Tokay et al., 2014). Moreover, statistical corrections are applied to minimize the misleading introduced by two or more particles passing through the sheet at the same time (Raasch and Umhauer, 1984). Another source of uncertainty is the quantization of drops caused by the introduction of particle size bins that may brings to relevant stochastic variations (Smith et al., 1993; Löffler-Mang and Joss, 2000).

The instrument places each particle in a 32×32 size versus velocity matrix, where bins are not regularly spaced. The size interval ranges from 0 to 25 mm, but the first two lower bins are not available because of low signal to noise ratio, so the minimum detectable signal increases to about 0.25 mm (Tokay et al., 2014). The velocity interval ranges between 0 and $20\,ms^{-1}$. The drop size distribution $N(D_j)$, where D_j is the equivolume drop diameter of the jth size bin, is then retrieved from the matrix data consisting in the number of drops of ith velocity and jth size $n_{i,j}$:

$$N(D_j) = \sum_{i=1}^{32} \frac{n_{i,j}}{A(D_j)\Delta t V_i \Delta D_j}, \tag{2.3}$$

where Δt is the sampling time, V_i is the measured raindrop fall speed at the ith velocity bin and ΔD_j is the jth size bin. $A(D_j)$ is the effective sampling area that also accounts the partially detected particles:

$$A(D_j) = 180\,mm \times (30\,mm - D_j/2). \tag{2.4}$$

Tokay et al. (2014) reports that the measurement accuracy is ± 1 size bin up to 2 mm, while for the particles bigger than 2 mm the accuracy is of ± 0.5 size bin (remembering that class size doubles at 2.8 mm).

Starting from the $N(D_j)$, the disdrometer software calculates precipitation parameters as rainfall rate, accumulated precipitation and reflectivity factor. Moreover, the kinetic energy of the drops and the meteorological optical range (MOR), that is an index of visibility, are retrieved. Adjustments are performed in case of solid precipitation.

Through size-velocity relations the instrument classifies the type of hydrometeors according to a scheme qualitatively similar to the one depicted in Fig. 2.3. The hydrometeor type discriminations are generated following three different classification codes. In the present work the METAR/SPECI weather code defined in *Code table 4678* (Manual on Codes, WMO-No. 306) is considered. The samples are divided in 1) drizzle (DZ), 2) drizzle with rain (RADZ), 3) rain (RA), 4) rain/drizzle with snow (RASN), 5) snow (SN), 6) snow grains (SG, i.e. embryonic graupel), 7) soft hail (GS, i.e. graupel) and 8) hail (GR). Each string, except for hail, is associated with a "-" in case of light precipitation, a "+" in case of heavy precipitation and with no additional signs in case of moderate precipitation.

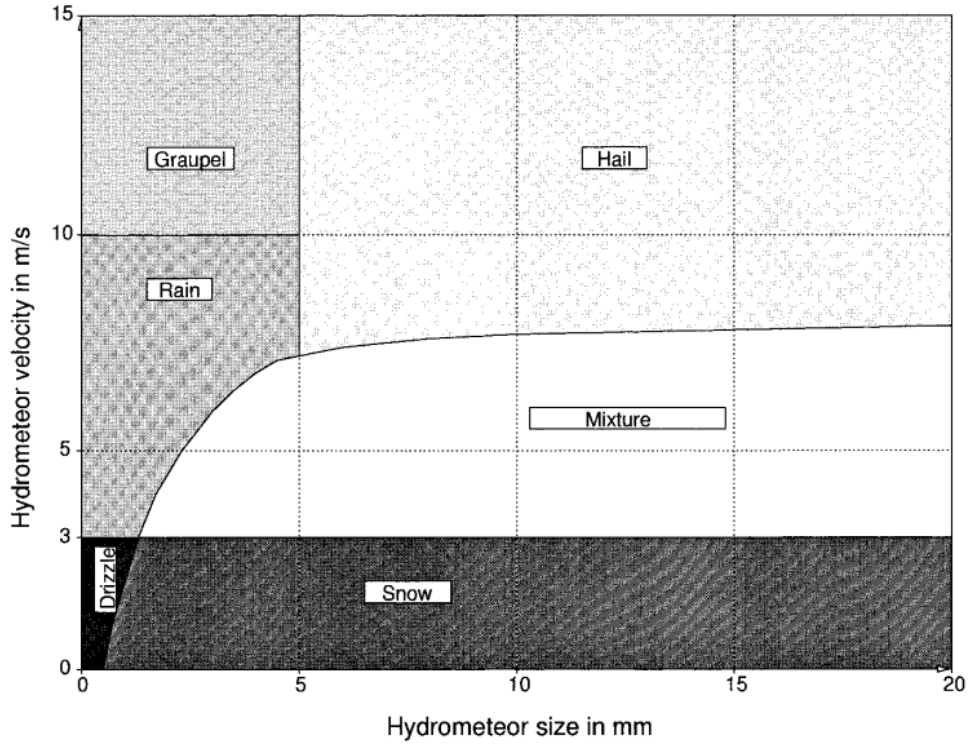

Figure 2.3: Hydrometeors classification scheme in function of size and velocity values. Source: Löffler-Mang and Joss (2000).

The manufacturer asserts an accuracy for precipitation rate measurement of ±5% for liquid and ±20% for solid occurrences. The type of precipitation identification has an agreement between the instrument and the "weather observer" greater than 97%.

2.2 Instruments site and climate

The radar and the disdrometer are located in the Po Valley, situated in Northern Italy. The valley is principally characterized by a climate classified as humid subtropical (Köppen), identified by hot, humid summers with frequent thunderstorms and foggy, damp and cool winters, with rare snow events. Precipitations are quite

equally distributed over the year, slightly peaked in spring and fall seasons, with a minimum in summer. On the city of Bologna (disdrometer site) precipitation reaches annually 785 mm (1991-2015 mean[1]).

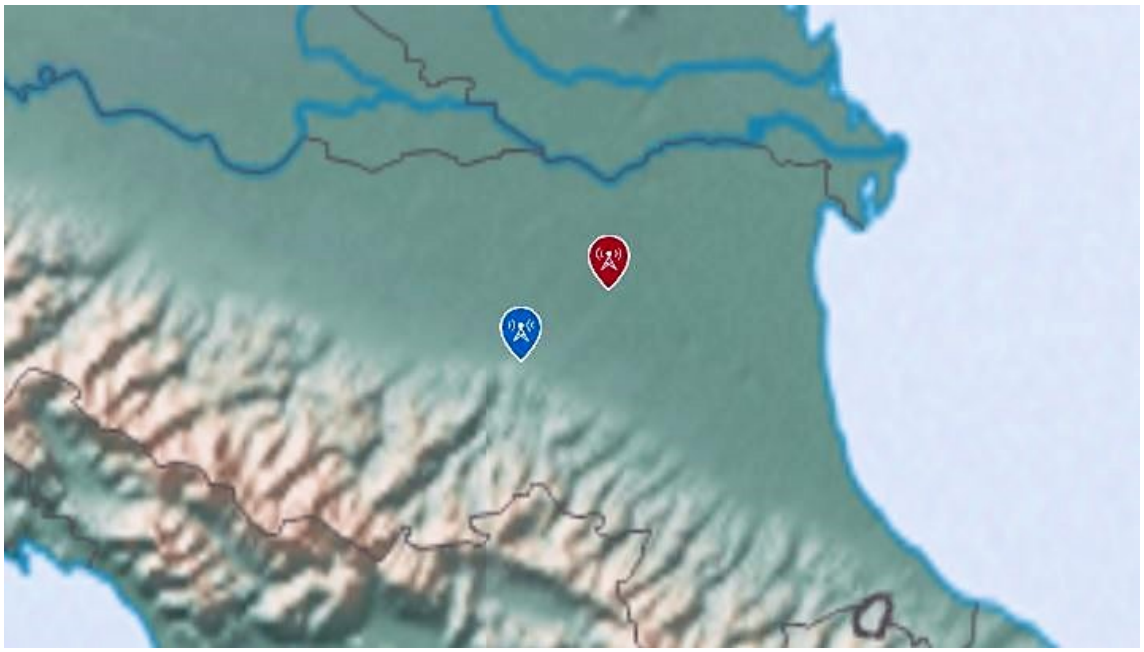

Figure 2.4: Morphology of the radar (red icon) and disdrometer (blue icon) sites.

The instruments sites are about 27.5 km away from each other (geodetic distance). The radar is located at an height of 31 m a.s.l. above a tower and the disdrometer is at 64 m a.s.l. on the roof of the Physics and Astronomy Department of the University of Bologna. The radar is placed in a rural context, while the disdrometer is in the city center of Bologna, surrounded by quite tall buildings. Buildings and, in addition, several radio wave interferences can't be neglected, because they degrade the radar low-elevation measurements. A qualitatively depiction of the morphology of the site is shown in Fig. 2.4. Hills and mountains are close to the disdrometer position, so the disdrometer site is surrounded by strong clutter

[1] Atlante climatico dell'Emilia-Romagna 1961-2015 - ARPAE

noise.

The portion of atmosphere between the instruments can assume low values of the refractivity gradient dN/dh. Statistics of that gradient are carried out by Alberoni et al. (1998) through radiosonde data collected at 00 UTC and 12 UTC. These data were acquired in the bottom layer of atmosphere at the radar site. The analysis shows that trapping conditions ($dN/dh < -157\,N/km$) are mainly found at night and during the summer.

2.3 Data

Two years of data are analyzed. However, some lacks of data reduces the dataset to about 11 months.

As stated above, the radar data are composed by PPI acquisitions every five minutes. The radar software generates hierarchical data subdivided by elevations and for each elevation the sampled variables are available. Each acquired variable have a matrix form composed by azimuth angles in the rows and ranges in the columns; therefore, every matrix element represents the radar volume at a certain azimuth and range. The azimuth resolution, both horizontally and vertically, is equal to 0.8° in the scan number 1 and 0.9° in the scan number 2 and 3. The range resolution is always 250 m.

The disdrometer software creates a sample every minute, containing the data of the minute just passed. The sum of the acquired and retrieved data are grouped in a "telegram" characterized by a string of text for every minute. The variables contained in each telegram string are schematized in Table 2.3. In case of detected particles by the disdrometer, the last row of the table is replaced by the 32x32 size

versus velocity matrix, resulting in 1024 values.

Data	Quantity
28.04.2020	Date
15:03:00	Time
0.000	Rainfall rate (mm/h)
53.69	Cumulative precipitation (mm)
0	Weather code SYNOP WaWa
NP	Weather code METAR/SPECI
C	Weather code NWS
-9.999	Radar reflectivity factor (dBZ)
20000	MOR Visibility (m)
18727	Signal amplitude of Laserband
0	Number of detected particles
20	Temperature in sensor (°C)
2.00	Heating current (A)
12.3	Sensor voltage (V)
0.000	Kinetic Energy
0	Snow intensity (mm/h)
<SPECTRUM>ZERO</SPECTRUM>	32×32 matrix of detected particles

Table 2.3: PARSIVEL^2 telegram containing data acquired by the instrument. Herein, a random minute with no precipitation detected is shown.

In the present Thesis the analyzed radar measurements are:

- the horizontal reflectivity factor Z_h,
- the linear depolarization ratio Z_{DR},
- the cross correlation coefficient ρ_{hv};

and the analyzed disdrometer measurement are the reflectivity factor Z retrieved by the DSD and the hydrometeor type classification.

Radar Z_h and disdrometer Z are comparable. Z_h is strictly linked to Eq. 1.33 that is a good approximation of Eq. 1.11. In fact, the error introduced with the approximation is not considered predominant in comparison with other uncertainties when comparing Eq. 1.33 to estimates from ground measurements of drop size distributions (Löffler-Mang and Blahak, 2001). From here on, the reflectivity factor associated with the radar and the disdrometer are defined respectively Z^{rad} and Z^{disd}.

2.4 Data matching and pre-processing

Only radar cells that correspond to the disdrometer position are considered for evaluating the matching between radar and disdrometer data. For choosing these radar cells, the following polar coordinates are set: 1) the azimuth angle of the radar which is in the direction of the disdrometer location, 2) the range r that corresponds to the distance between the instruments following the earth geodesics. This azimuth angle is equal to 231.1° and the range is about 27.505 km.

As a first approximation the radar cell is a volume defined by $r \sin(\beta_{-3dB})$ times the range resolution. As a result, the radar cell above the disdrometer has approximately a volume equal to $4.67 \times 10^{-2}\, km^3$. The azimuth resolution is about 432 m. The height of the radar volumes above the disdrometer depends on the radar elevation. Applying the Eq. 1.23, for the first three elevations (0.5°, 1.4°, 2.3°) the cells are centered at a height of 252 m, 684 m and 1116 m, respectively.

The radar data time acquisition of a cell is almost instantaneous ($\ll 1\, s$),

while the resolution of the disdrometer is 1 minute. The temporal matching between the two instruments is performed choosing the disdrometer sampling which contains the radar acquisition.

In addition data are treated through filtering processes.

Radar data are filtered through a series of algorithms developed by the SIMC, based on the application of thresholds to some radar variables. To suppress clutter and interferences, the Doppler quantities V_{rad} and W_{rad} and the variability of reflectivity factor and linear depolarization ratio are used. In case of lack of Z_{DR}, a fuzzy logic scheme is set. This cleaning process operates on the Z^{rad} and rejects bad quality values. As a consequence, when the Z^{rad} is rejected the other corresponding radar variables are rejected. An additional filter is developed through the previous described algorithm of hydrometeor type classification which, when applicable, gives an indication of the presence of clutter, anomalous propagation or biological scatterers.

Disdrometer data are affected by three main sources of uncertainty: 1) strong winds leading to a misclassification of particles, 2) particles falling through the edges of the sample area and 3) splashing effects from particles hitting the instrument surfaces, breaking up into smaller particles, and then passing through the sampling area (Friedrich et al., 2013). The strong wind misclassification is treated following the scheme proposed by Friedrich et al. (2013): the sampling minute completely removed if large ($d > 5\,mm$), slow-falling ($v < 1\,ms^{-1}$) particles are observed. Margin fallers are already partially corrected using the sampling area definition as in Eq. 2.4. Splashing effects are not treated because mostly related to small drops (not relevant effects in reflectivity factor calculations) and because the disdrometer is designed to minimize splashing. In addition, samplings are rejected if less than

10 particles are detected during the minute of acquisition (Tokay et al., 2014).

Chapter 3

Analysis and Results

This Chapter reports the analysis and the results achieved in the present Thesis. In Section 3.1 a comparison between the measured reflectivity factors Z^{rad} and Z^{disd} is developed; then, a sensitivity analysis is realized. In Section 3.2 starting from the discrimination between stratiform and convective precipitation obtained by the disdrometer, distributions of Z^{rad}, Z_{DR} and ρ_{hv} are analyzed. Section 3.3 describes the comparison between the hydrometeor type classification of the two instruments. Lastly, in Section 3.4 the case study of a thunderstorm event is reported.

3.1 Reflectivity factor comparison

Reflectivity factor comparison between Z^{rad} and Z^{disd} is performed to analyze the correlation between the radar and the disdrometer. Several issues are related to this comparison. Kalina et al. (2014) considers a rain drop of 1-mm diameter and a terminal velocity of 4 ms^{-1}, if the drop is at a height of 1 km when the radar observes it, it will reach the ground about 4 min later. Assuming the presence of a mean

horizontal wind speed of 10 ms^{-1}, the same drop will be advected at about 2.5 km downstream from the point in which it was observed by the radar. This example underlines the possibility of a mismatch between the two instruments observations. Moreover, DSD evolves accordingly to the processes described in Subsection 1.2.1. Other processes affect the DSD evolution, for example the vertical variations of pressure (List et al., 2009; Porcù et al., 2013). Another source of uncertainty is the different extension of the sampling domains. In fact, the volume of the radar cell ($\simeq 47 \times 10^6\, m^3$) is larger than the disdrometer surface ($5.2 \times 10^{-3}\, m^2$) and a non-uniformity precipitation regime inside the radar volume may lead to misleading results.

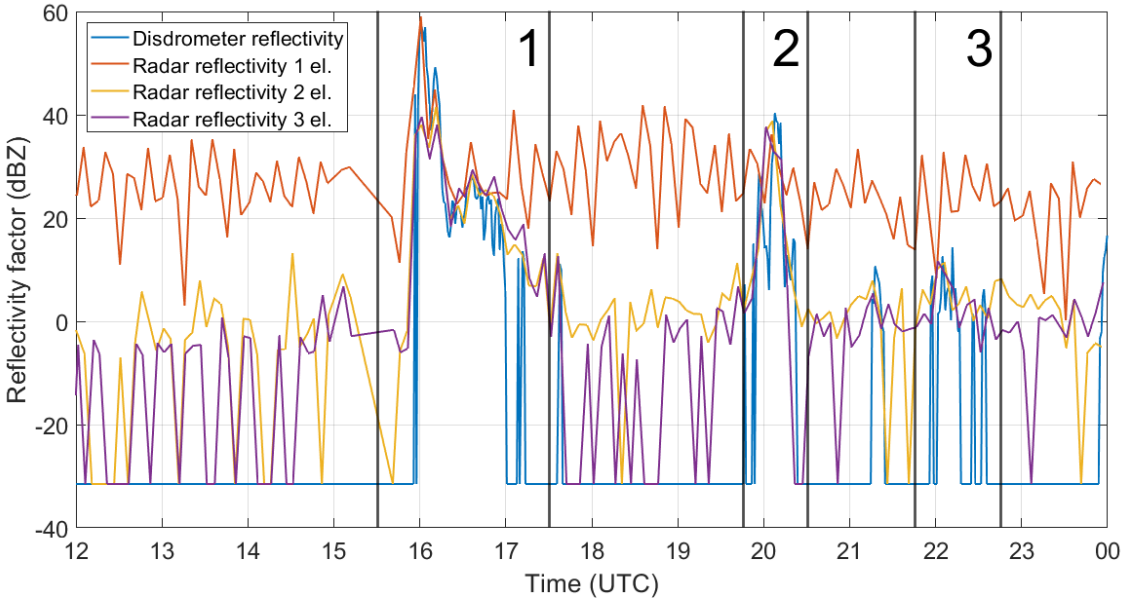

Figure 3.1: Radar and disdrometer reflectivity factor comparison on May 28th 2019 in the time interval 12-00 UTC. Radar data of the three elevations are unfiltered. No. 1,2 and 3 in the plot identify the three precipitation events.

For example, if the precipitation covers only a fraction of the radar cell and this fraction does not contain the disdrometer site, the precipitation is detected only

by the radar. Another example could be represented by the "core" of a convective system only intercepted by the radar volume.

To examine the impact of the antrophogenic noise, 12-h of disdrometer and unfiltered radar reflectivity factor data are analyzed (Fig. 3.1). In particular, the radar data are measured in the cell above the disdrometer at the first three radar elevations. The elevation angles that characterized these three radar elevations are 0.5°, 1.4°, 2.3°. The cells of these elevations are centered at a height of 252 m, 684 m and 1116 m, respectively. The analysis highlights the presence of a background noise (clutter) whose generation is ascribed to interfering antennas and tall buildings in the surrounding of the disdrometer site. Figure 3.2 shows the unfiltered PPI of the first radar elevation, where the white circle identifies the site of the disdrometer. This PPI has been sampled on May 28th 2019 at 14:00 UTC in clear sky conditions in the disdrometer surroundings. Interfering antennas cause the radial signal that crosses the disdrometer site. The intensification of the noise at the disdrometer location may be due to the presence of tall buildings. As a result, when no precipitation is detected by the disdrometer, the first elevation echo oscillates around 20-30 dBZ. The second and the third elevations are less affected by noise and their echo fluctuates between the minimum detectable signal (-31.5 dBZ) and slightly positive values. Conversely, the disdrometer signal is noise free.

Figure 3.1 highlights three precipitation events occurred on May 28th 2019. These events are characterized by different intensities and they are interrupted by rain-free periods. Event no. 1 is detected in its most intense phases by both the disdrometer and all the radar elevations, while the radar echo of the first elevation is degraded by the noise for weaker precipitation intensities. In events no. 2 and 3, the noise at the first elevation totally overcomes the meteorological signal, so data

retrieved by this elevation are not available. The event no. 3 is characterized by very low intensities, in fact values close to 0 dBZ represent drizzle precipitation. This event is not discerned by the second and the third elevation from noise.

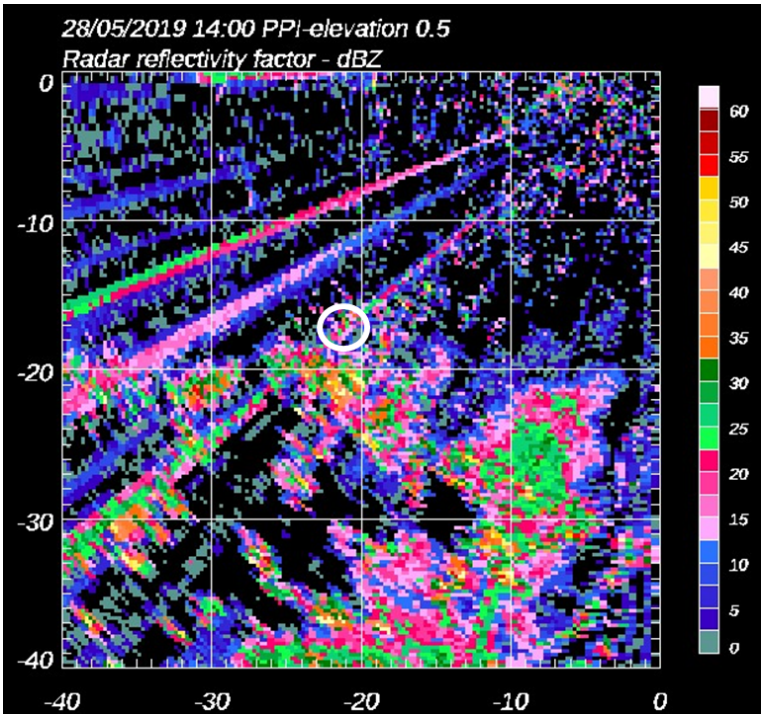

Figure 3.2: Unfiltered first radar elevation PPI sampled on May 28$^{\text{th}}$ 2019 at 14:00 UTC. White circle identifies the disdrometer site. Axes values (km) represent the distance from the radar.

Despite the fail in measuring during this event may be of interest for other analyses, it does not affect the quality of the present study which does not focus on drizzle precipitation.

Fig. 3.3 shows a scatterplot between the filtered data of this elevation and the disdrometer ones. The scattered data exhibit a tail of quite constant radar values for low disdrometer reflectivities. This kind of tail, enclosed in the red box, represents (clutter) which is not rejected by the filtering scheme applied to the radar data.

Values of the tail (20-30 dBZ) are consistent with the noise observed in non filtered radar data in Fig. 3.1. This issue arises because the radar filter should be valid under as many conditions as possible in order to clean a large spatial domain. The single radar cell over the disdrometer is affected by the urban landscape of Bologna and it is difficult to clean.

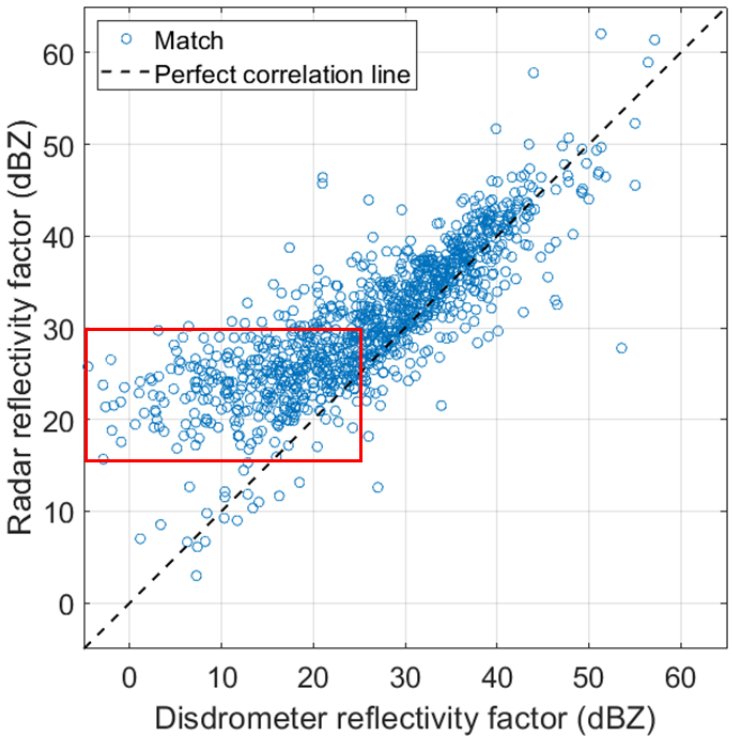

Figure 3.3: Scatterplot of Z^{disd} and filtered Z^{rad} measured at the first elevation. The black dashed line represents the perfect correlation line between the two instruments data. Some of the data enclosed in the red box show a tail of clutter occurrences.

However, since the 11th August 2020 the radar azimuth which is in direction of the disdrometer was cleaned due to the frequency shift of interfering antennas. The resulting background noise is now weaker of about 10 dBZ; thus, the first elevation may become more useful for future comparison analyses. First elevation data are

important because they are the closest acquisition to the surface and the DSD experiences the smaller modification possible reaching the ground.

With the aim of having a signal less affected by noise compared to the first elevation one, the data of the second radar elevation are used. For the comparison, a scatterplot similarly to the previous one is generated. A total of 11483 radar and disdrometer matches are found. From the analysis are removed matches where at least one of the instruments does not detect precipitation. This removal procedure is made necessary to remove the samplings where the radar or disdrometer filter fails compromising the comparison. However, no-noisy data may be lost if the precipitation system covers the fraction of the radar domain which does not include the disdrometer site. Rejected data are approximately 70% of the whole matches. Occurrences where the disdrometer does not detect precipitation and at the same time the radar measures no precipitation or small intensities (<10 dBZ) represent the 65 % of these rejected matches. The remaining 5% excluded data possibly refers to no-noisy data that are acquired in conditions of partially covered radar cell. The result of the comparison is shown in Fig. 3.4.

The quality of the correlation is evaluated through the Pearson correlation coefficient (CC) applied to the N scattered data of Fig. 3.4. CC is defined as:

$$CC(Z^{disd}, Z^{rad}) = \frac{1}{N-1} \sum_{i=1}^{N} \left(\frac{Z_i^{disd} - \mu_{Z^{disd}}}{\sigma_{Z^{disd}}} \right) \left(\frac{Z_i^{rad} - \mu_{Z^{rad}}}{\sigma_{Z^{rad}}} \right), \tag{3.1}$$

where $\mu_{Z^{disd}}$ and $\sigma_{Z^{disd}}$ are respectively the mean and the standard deviation of Z^{disd}, and $\mu_{Z^{rad}}$ and $\sigma_{Z^{rad}}$ are the mean and the standard deviation of Z^{rad}. Here, Z^{rad} is referred to the reflectivity factor of the second elevation. The result shows a $CC = 0.84$, that is a good result considering the several sources of uncertainty

involved in this comparison, starting from the different sampling volume. The linear fit applied to the scattered data shows a slope of 0.83 and a vertical intercept of about 4.2 dBZ.

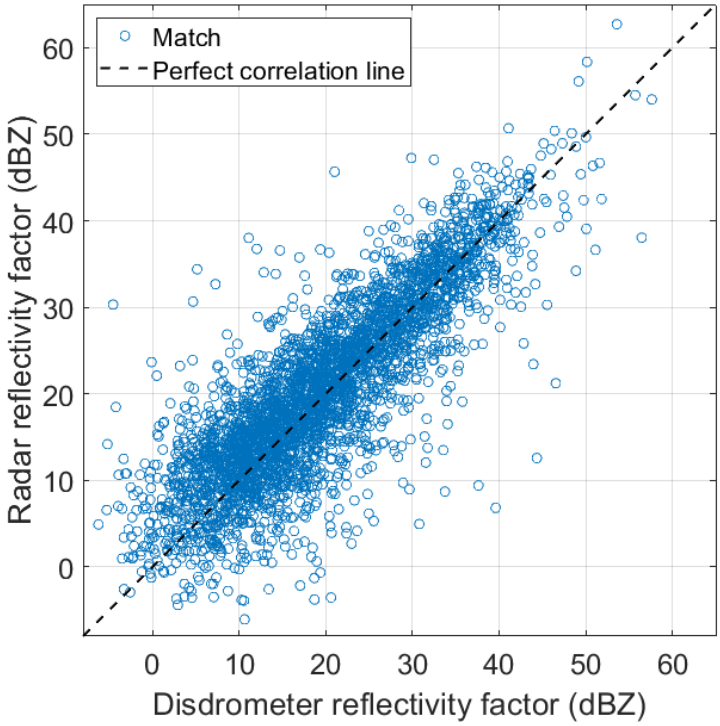

Figure 3.4: Scatterplot of Z^{disd} and filtered Z^{rad} measured at the second elevation. The black dashed line represents the line of perfect correlation between the two instruments data.

The comparison between the radar third elevation (centered at about 1116 m) and the disdrometer data points out a good agreement of the instruments measurements too, even if a greater dispersion of data is observed (CC=0.79). The processes affecting the DSD of the hydrometeors during the descent cause the worsening of the correlation when the third elevation data are used for the comparison. This worsening may be influenced by the advection of the hydrometeors during the fall. A sensitivity test between the second and the third elevations of the radar is

developed. Groups of radar cells (e.g. 7x7 or 9x9) centered on the disdrometer of the second and the third radar elevation are selected. In addition, group of cells of the third elevation slightly shifted from the one centered above the disdrometer are retrieved. The values of each group of cells are averaged and a comparison is performed between the mean value of the second elevation and various mean values of the third elevation. Some of the shifted groups of the third elevation show a better correlation with the second elevation in comparison to the centered third elevation. This result highlights that advection of hydrometeors is a not negligible process during the fall.

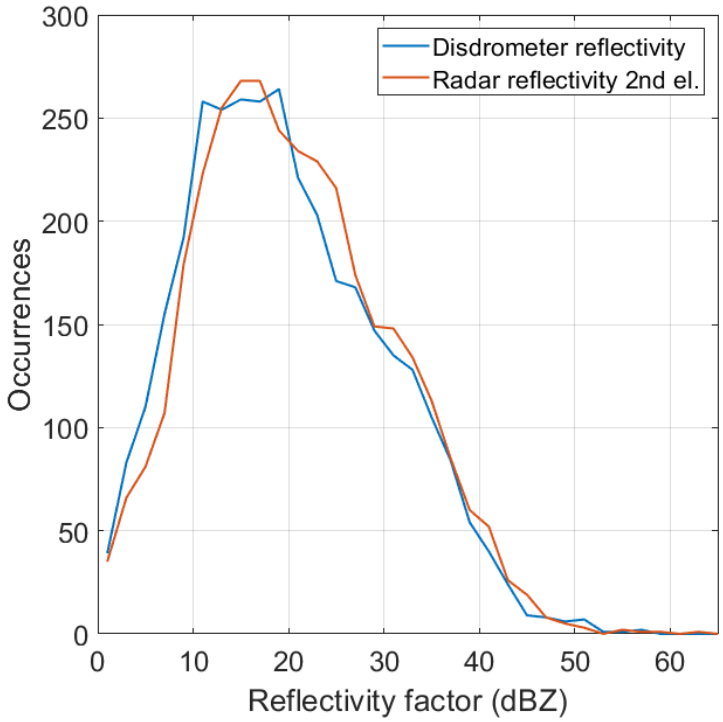

Figure 3.5: Distributions of matched Z^{disd} and filtered Z^{rad} measured at the second elevation. The bins range from 0 to 64 dBZ; bin size is constant and equal to 2 dBZ.

Therefore, the second elevation is the best possible choice for the comparison

with the disdrometer. The distributions of the reflectivity factor data of the second radar elevation and the disdrometer are plotted in Fig. 3.5. The sampling matches are nearly the same of the ones showed in the previous scatterplot (Fig. 3.4). In addiction, since negative Z refers to a small number of mainly noisy samplings (see again Fig. 3.4), matches data are excluded when at least one of the two instruments measures negative Z. Both the distributions have a peak of number of occurrences between 10 and 20 dBZ; the radar distribution shows a sharper peak. The distributions especially differ from each other in [0-10] dBZ and in [20-30] dBZ intervals. For $Z > 35$ dBZ, the number of samplings of the two distributions are similar. The radar records have a median value of 19.3 dBZ, the disdrometer records of 18.4 dBZ.

Departures from the perfect correlation line shown in Fig. 3.4 and different shape of distributions highlighted in Fig. 3.5 may have several causes. Five sources of uncertainty are hypothesized: 1) different calibration of the instruments, 2) evaporation of falling hydrometeors, 3) the melting layer located close to the height of the second elevation volume, 4) drifting of particles during the fall and 5) stronger precipitation covering only a fraction of the radar cell that does not include the disdrometer site. The first cause is supported by the scatterplot and the distributions just shown, where the radar samplings generally assume larger values compared to the disdrometer ones. The second cause seems to occur in some circumstances of light rain, because, as seen in the Chapter 1, for small drops the evaporating process is more efficient. The third cause is observed in conditions where the frost point, i.e. the temperature at which the water vapor is saturated over an ice surface, is located in proximity of the height of the second elevation volume. In Section 3.3 an example of the third cause occurrence is reported. The fourth cause is detected when the particles are advected horizontally during the fall. This issue is described

at the beginning of the Section through the study of Kalina et al. (2014) and in the case study analysis (Section 3.4.1). The fifth cause may occur when the precipitation field is not uniform. Remembering that Z is the sixth moment of the distribution, large drops are the most relevant in its computation (Fig. 1.5). Hence, if strong precipitation are detected only by the radar volume, discrepancies between the measurements of the two instruments arise. This cause is observed in the first analysis of the next Subsection (Fig. 3.6).

Several tests are performed to study if other meteorological or non meteorological factors could be the cause of the differences observed in the distributions. As a first test, different distributions are generated for radar scan no. 1 compared to scans no. 2 and 3 (scans defined in Table 2.2). The radar signal for each cell of these last scans results from a larger number of integrated pulses compared to the first one. The hypothesis is that the stronger signal may cause higher values of Z^{rad}. Another test generates distributions for filtered data and for double filtered data. "Double filtered" means that in addition to the filter on Z^{rad} values, a second filter retrieved by the algorithm of hydrometeor-type classification (Section 2.1.1) is applied. This results in an additional data rejection since the algorithm classifies some samplings as clutter/anomalous propagation and biological scatter. For implementing a third test, only sampling matches where low variability of precipitation regime are distributed. In fact, sampling matches are chosen with a precise criterion: in the matches, the disdrometer sampling must be classified as stratiform and it must be the central sample of a 5-min block of consecutive stratiform rain. The purpose is to have a comparison where the radar cell is the most evenly covered as possible.

The results of these tests do not bring evidence of dependence on the screened factors.

3.1.1 Sensitivity analysis

Sensitivity analyses are developed to study the consequences of choosing different spatial radar domains or disdrometer time shifts.

Firstly, groups of cells from 3x3 to 9x9 of the second radar elevation centered on the disdrometer location are selected. The aim is to analyze if using these groups, instead of the single cell, results in a better correlation with the disdrometer data. The spatial extension of the radar groups spreads from about 750 m in range, 1.2 km in azimuth and 432 m in height for 3x3 groups to about 2.5 km in range, 3.6 km in azimuth and 432 m in height for 9x9 groups. The groups of values are averaged so that an unweighted mean of 9 samples is applied to 3x3 groups up to a mean of 81 samples to 9x9 groups. Matching samples are excluded from the comparison if the 9x9 group contains NaN values or if the central radar cell or the disdrometer have negative Z values. Matches with the occurrence of the NaN values are excluded because the comparison of different groups would result as non-significant.

The remaining values are arranged in the distributions shown in Fig. 3.6. All the group distributions show consistency compared to the single cell and the disdrometer ones. Overstimation and underestimation of occurrences in the same intervals of the single cell distribution are observed. However, the deviation from the distribution of the disdrometer data increases with increasing number of radar cells. In particular, larger is the initial domain of cells larger is the underestimation of low-reflectivity occurrence. This trend is explained through the following consideration. A larger domain is more likely to intercept the more intense section of a quite localized precipitation event. Since Z shows an exponential behavior, the group averages are highly influenced by the cells where intense precipitation is occurring.

As a result larger groups of cells tends to have higher Z values compared to the disdrometer and the single cell data. Hence, the signal of the central cell is the most accurate for the comparison with the disdrometer signal.

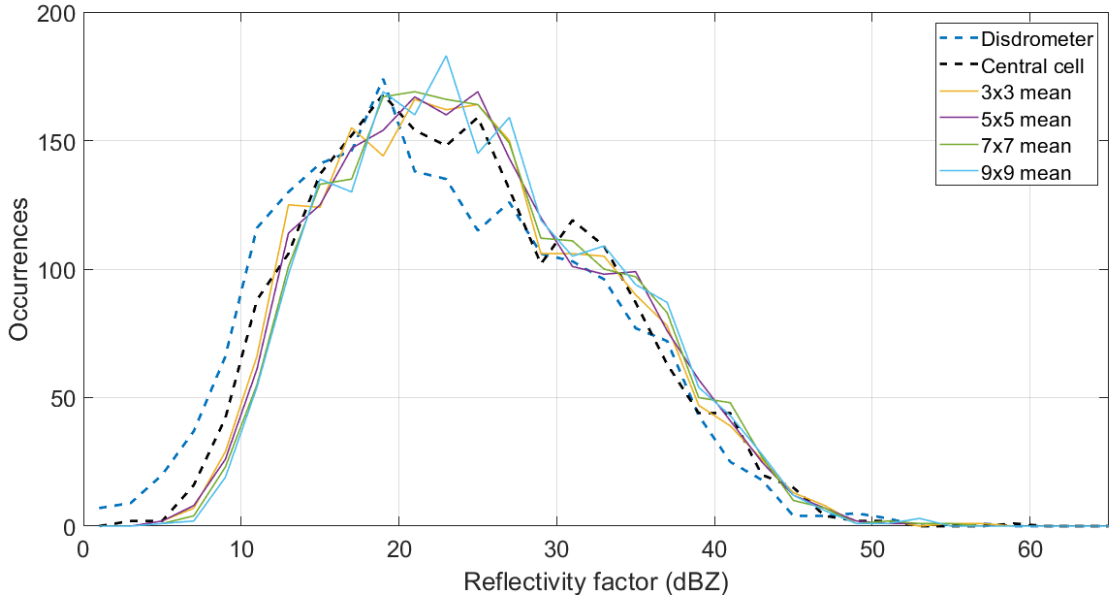

Figure 3.6: Sensitivity analysis between filtered radar groups of different sizes of cells. "Central cell" refers to the single cell above the disdrometer. The bins range from 0 to 64 dBZ; bin size is constant and equal to 2 dBZ.

A further analysis is performed starting from the 3x3 group of cells centered on the disdrometer, where each of these cells are considered as a single cell. This results in 9 different distributions (including the one centered on the disdrometer location) to compare with the one of the disdrometer.

Figure 3.7 shows that these distributions appear to slightly differ from each other. This confirms the goodness of using only the central cell when the full filtered dataset is used for the comparison. Possible further analyses may look for the best correlation through the shifting of groups of cells instead of choosing "concentric" groups centered on the disdrometer location.

When no ice phase hydrometeors are detected, the terminal velocity of the particles are ranged from about 1 ms^{-1} to 10 ms^{-1}. This means that the drops observed by the second elevation of the radar take tens of seconds up to minutes to reach the disdrometer. This consideration suggests an analysis performed by shifting forward (+1, +2 and +3 min) the disdrometer samplings. For example, when the +1 minute shift is applied, the radar data is matched with the disdrometer acquisition of the following minute compared to the radar acquisition time.

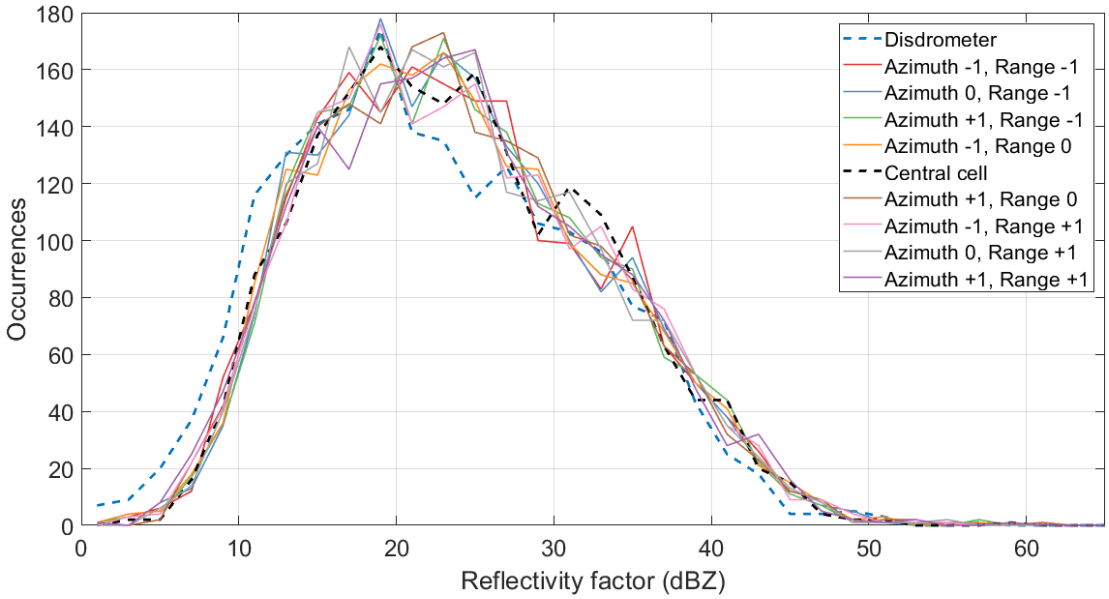

Figure 3.7: Sensitivity analysis among filtered neighboring cells. In legend ±1 means a cell shift in azimuth and/or in range within the radar domain. The bins range from 0 to 64 dBZ; bin size is constant and equal to 2 dBZ.

Pearson correlation coefficients are calculated for the various shifts and they are shown in Table 3.1. Results reveal that a shift in the disdrometer samplings is a good improvement to the CC. In fact, +1, +2 and +3 minutes shifts bring to a slightly better agreement between the instruments data. This trend is explained by considering that, in the dataset, stratiform events characterized by long and quite

constant reflectivity series have a relevant weight. Actually, the results are different when only matches where both instruments measures heavy precipitation intensities are retained ("Heavy" row in Table 3.1).

Data	+0 min	+1 min	+2 min	+3 min
All	0.84	0.87	0.88	0.86
Heavy	0.54	0.67	0.59	0.52

Table 3.1: Pearson correlation coefficient between the radar second elevation and the disdrometer data. The "All" row include the same dataset used for the calculation of the correlation coefficient in the scatterplot (Fig. 3.4); "Heavy" row include samplings where both instruments measures reflectivity factors larger than 35 dBZ. Column names refer to the time shift applied to the disdrometer data in comparison with the radar data.

The threshold used to identify heavy precipitation is $Z > 35\,dBZ$ (typically used in radar-meteorology). The correlations are poorer as a consequence of the usual stronger variability in heavy precipitation patterns. However, +1 and +2 minutes shifts have again a better correlation with radar data compared to no-shifted disdrometer data. In particular +1 minute shift shows a significantly larger correlation (0.67).

3.2 Stratiform/Convective discrimination

A stratiform and convective precipitation discrimination is applied to the disdrometer samplings. The classification is developed through the method proposed by Caracciolo et al. (2006). This method is settled for continental mid-latitude rain and it is based on M_4, M_5 and M_6, respectively the fourth, fifth and sixth moments of the DSD. These moments are retrieved from the general statistical moments M_n

formulation:

$$M_n = \int_0^\infty N(D) D^n dD = \sum_{i=1}^{32} N(D_i) D_i^n, \tag{3.2}$$

where n is the order of the moment and the discretization is made necessary by the discretization of PARSIVEL^2 size bins (i=32). The higher the considered moments are, the lower the underestimation of the small drop amount, that is an issue for the PARSIVEL^2 (Park et al., 2017), will be. The sixth moment M_6 is the reflectivity factor introduced in Subsection 1.2.2.

These moments are used to retrieve the discrimination line for classifying the convective and stratiform precipitation:

$$1.635\Lambda - \mu = 1, \tag{3.3}$$

where Λ and μ are the parameters of the gamma distribution defined as

$$\Lambda = M_4 M_5 / (M_4 M_6 - M_5^2), \tag{3.4}$$

$$\mu = (\Lambda M_6 / M_5) - 6. \tag{3.5}$$

Λ and μ are equivalent to the ones in Eq. 1.6.

Considering a (Λ , μ) diagram, the samplings that lie above the line are classified as stratiform while the others are classified as convective. This is a general distinction that does not discriminate the weak convection as well as the strong aggregation precipitation often characteristic of the stratiform events. However, this discrimination has a physical meaning considering that the stratiform classified samplings generally have spectra dominated by many small drops compared

to convective ones. Moreover, there is a coherence between convective and stratiform classification obtained through this method and others one, here not reported, based on rainfall rate (Bringi et al., 2003) and peak diameter considerations (Caracciolo et al., 2006), where the peak diameter D_p corresponds to the maximum DSD concentration.

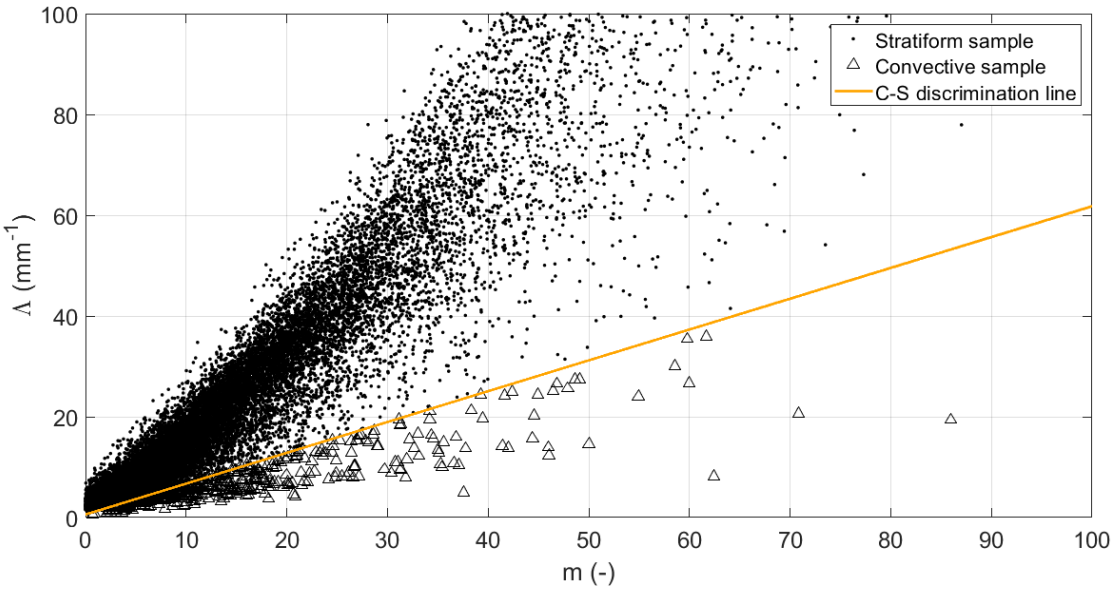

Figure 3.8: Convective and stratiform precipitation discrimination obtained through Caracciolo et al. (2006) scheme. C-S discrimination line is equal to Eq. 3.3.

In Fig. 3.8 the qualitatively results of this discrimination is shown. The Figure reports almost all the disdrometer precipitation occurrences. The dataset contains 489 convective precipitation samples and 20331 stratiform precipitation ones. Radar and disdrometer data are matched with the same criteria used for the distributions in the previous Section. Therefore, available dataset reduces to 60 convective and 3377 stratiform values. The effects of the disdrometer discrimination on the parameters Z^{rad}, Z_{DR} and ρ_{hv} of the second radar elevation are now evaluated.

Two distributions of Z^{rad} are generated. One distribution is created by collecting the Z^{rad} values that are matched with the samples classified as convective by the disdrometer (blue histogram in Fig. 3.9).

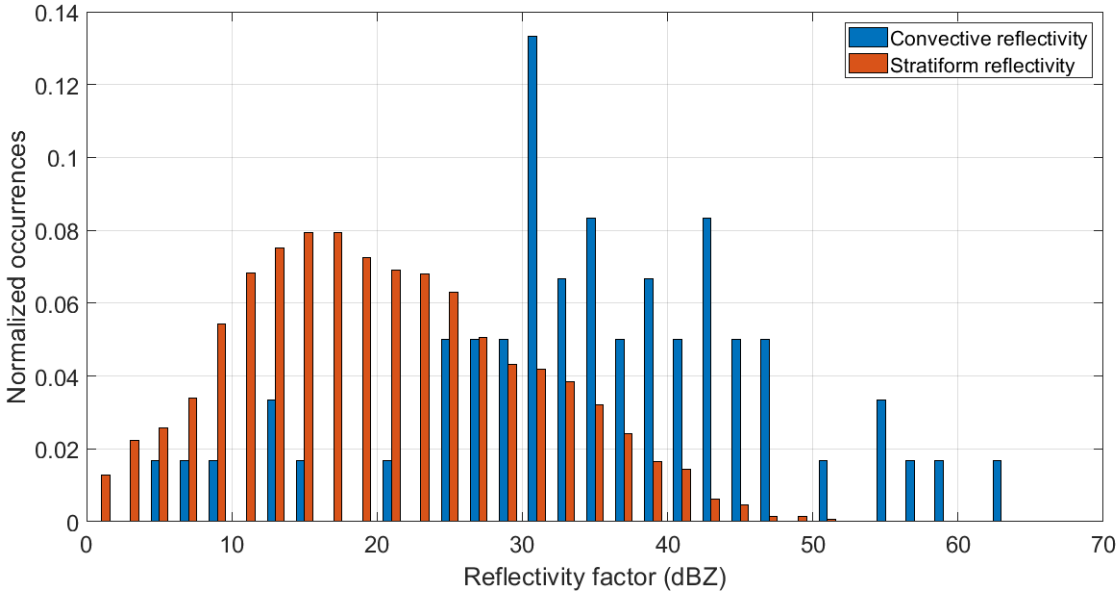

Figure 3.9: Z^{rad} normalized distributions retrieved from the filtered samplings of the radar second elevation. Blue histogram shows normalized distributions of Z^{rad} matched with samplings classified as convective by the disdrometer; instead, red histogram shows normalized distributions of Z^{rad} matched with samplings classified as stratiform by the disdrometer. The bins range from 0 to 64 dBZ; bin size is constant and equal to 2 dBZ.

The other distribution is created by collecting the Z^{rad} values matched with the stratiform disdrometer samplings (red histogram in Fig. 3.9). These distributions are normalized by considering the total number of stratiform and convective occurrences. Results display larger Z^{rad} values for the convective samplings compared to the stratiform ones. Median values are equal to 34.6 dBZ for the convective distribution and to 19.3 dBZ for the stratiform distribution. In Fig. 3.9 some unusual values can be noticed in both the distributions. In fact, a small percentage

of convective samples have values ranging from about 5 dBZ to 15 dBZ. This result could be explained by the high spatial and temporal variability of the precipitation in convective structures. In fact, close to changing conditions of the precipitation patterns, the two instruments may detect two different patterns. Conversely, for stratiform samplings there is a small percentage of Z^{rad} values larger than 35 dBZ. This could happen for the same reasons that cause the occurrence of low Z^{rad} in convective distributions. Moreover, another cause of these large Z^{rad} could be related to a misleading in the classification of stratiform occurrences by the algorithm. An example of this last issue is described in Section 3.4.

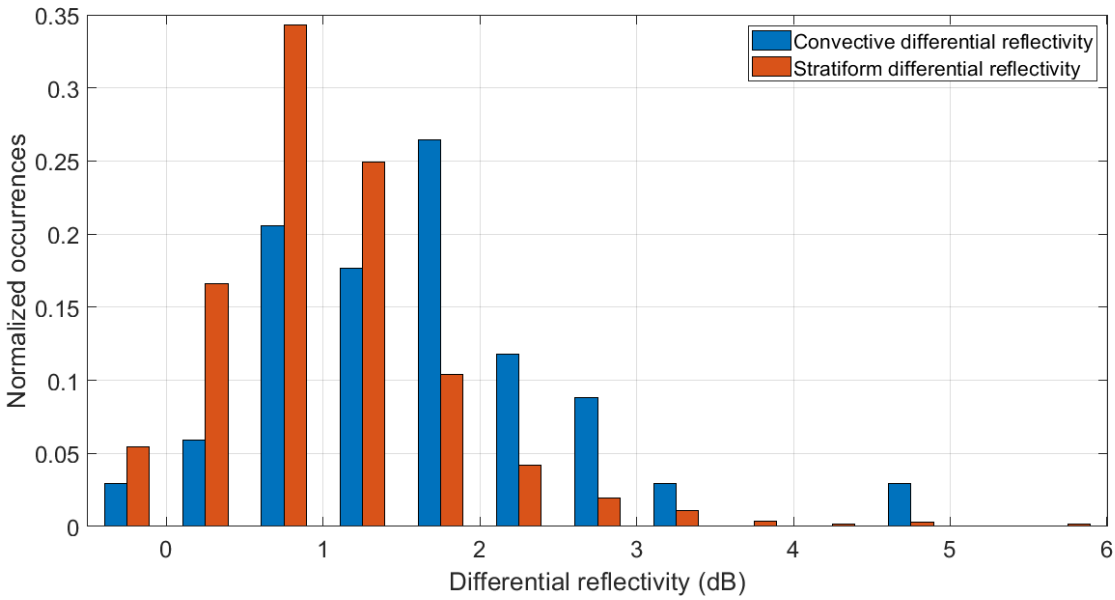

Figure 3.10: Z_{DR} normalized distributions retrieved from the filtered samplings of the radar second elevation. Blue histogram shows normalized distributions of Z_{DR} matched with samplings classified as convective by the disdrometer; instead, red histogram shows normalized distributions of Z_{DR} matched with samplings classified as stratiform by the disdrometer. The bins range from -0.5 to 6 dB; bin size is constant and equal to 0.5 dB.

Following the same criterion, convective and stratiform distributions for Z_{DR} are created (Fig. 3.10). The distributions contain 34 convective values and 2123 stratiform ones. The dataset is reduced of about the 60% in comparison with the one used for Z^{rad}. This reduction is caused by the fact that only two radar scans out of three calculate Z_{DR}. Moreover, a small number of clearly not-meteorological values of Z_{DR} that are not included in [-0.5, 6] dB interval are rejected. Convective distribution shows a peak for larger Z_{DR} values in comparison to the stratiform one. The median for the convective samples is 1.5 dB, while for the stratiform samples is 0.9 dB. This is an expected result, because during convective precipitation events large oblate drops are common, causing higher Z_{DR} values. The presence of unusual values are related to the same issues pointed out in the previous Z^{rad} analysis: 1) the high spatial and temporal variability of the precipitation in convective structures, 2) the misleading in the classification of stratiform occurrences by the algorithm. In addiction, a known little mismatch between horizontal and vertical beams of the radar could increase the noise in Z_{DR} data.

Lastly, the correlation coefficient ρ_{hv} distribution is analyzed. A known noise affects this parameter reducing the number of good-quality convective samples to a dozen out of 60. Hence, the causes of the noise are studied. Figure 3.11 depicts the distribution of the stratiform samplings, where a total of 1655 records are retained. Clearly not-meteorological occurrences that are not included in the [0.7-1] interval are excluded. Typical ρ_{hv} related to meteorological echoes assume values between 0.9 and 1. Normally, correlation coefficients smaller than 0.9 are associated to the melting layer that somewhere is detected in the radar dataset, as described in the next Section. However, the magnitude of the melting layer effect on ρ_{hv} measurements is not evaluated.

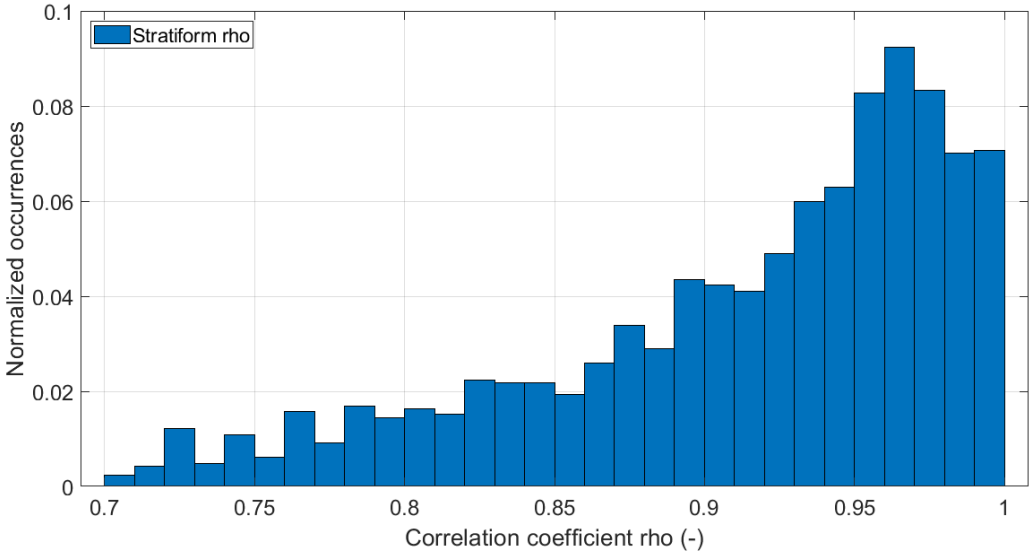

Figure 3.11: The histogram shows normalized distributions of radar second elevation filtered ρ_{hv} matched with samplings classified as stratiform by the disdrometer. The bins range from 0.7 to 1; bin size is constant and equal to 0.01.

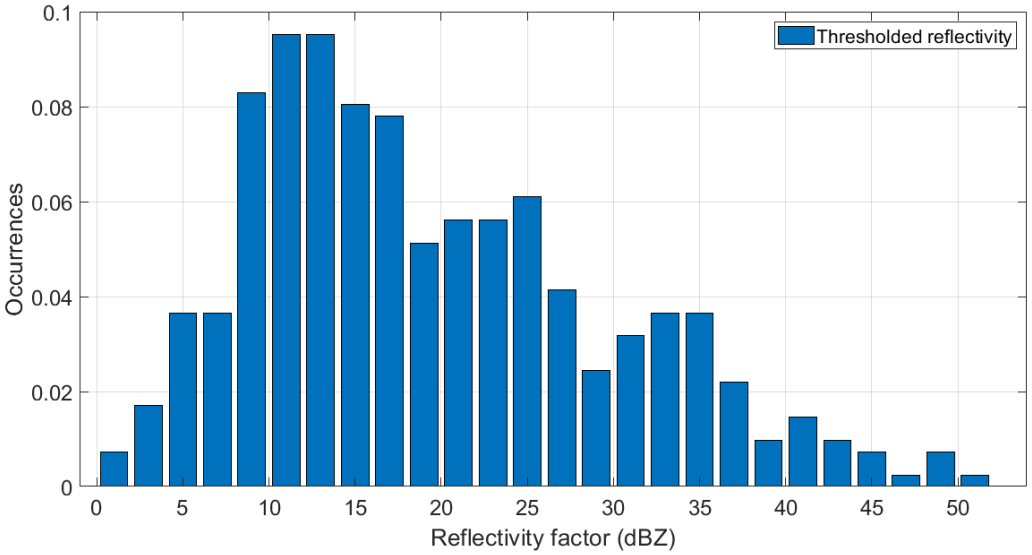

Figure 3.12: Reflectivity factor distribution of stratiform matches, where the ρ_{hv} ranges between 0.8 and 0.9.

In Fig. 3.11 a significant number of values smaller than 0.9 are shown, that may are related to the known noise. This noise is stronger in case of low reflectivity factors, so Z^{rad} distribution of radar matches with occurrences where ρ_{hv} is included in the [0.8-0.9] interval is generated (Fig. 3.12). The histogram shows a distribution that peaks at lower values compared to the whole stratiform dataset reported in Fig. 3.9 and that has a smaller median value (17.3 dBZ). Therefore, noise affecting small Z^{rad} may be one of the cause of ρ_{hv} values smaller than 0.8.

3.3 Classification comparison

The classification of the hydrometeor types is computed by the two instruments through the procedures and the algorithms described respectively in Subsection 2.1.1 for the radar and in Subsection 2.1.2 for the disdrometer.

Matching class	Radar classes	Disdrometer classes
Rain	RA	(+/-)DZ, (+/-)RADZ, (+/-)RA
Heavy rain	BD, HR	+RA
Hail	GR, RH	(+/-)GS, (+/-)GR
Snow	DS, WS, CR	(+/-)RASN, (+/-)SN, (+/-)SG

Table 3.2: Criterion of the matching classes for the radar and the disdrometer samples. Codes of radar and disdrometer classes are the same introduced in Section 2.1.

A contingency table is generated by comparing the samplings of the second radar elevation of the cell above the disdrometer and the samplings of the disdrometer. Four classes are defined in this table: 1) rain, 2) heavy rain, 3) hail and 4) snow. These classes are created by sorting the classifications retrieved by the two

instruments as shown in Table 3.2. The different principles used by the instruments to classify the hydrometeors do not allow to set up a more rigorous criterion. Matches are excluded from the analysis if: 1) the Z^{rad} value is rejected by the radar filter; 2) the classification algorithm of the radar labels the radar sample as clutter/anomalous propagation or biological scatter; 3) the disdrometer is not able to classify the sample. A category concerning no-precipitation occurrences is not added to the contingency table, because the noise in radar acquisitions does not allow to evaluate this type of class.

		R A D A R			
		Rain	Heavy rain	Hail/Graupel	Snow
D I S D R O M E T E R	Rain	1761	27	20	204
	Heavy rain	37	8	8	11
	Hail/Graupel	1	3	1	1
	Snow	0	0	4	2

Table 3.3: Contingency table of the data of the second radar elevation and the disdrometer.

Table 3.3 reports the results of the comparison between the radar and the disdrometer classifications. The sum of the occurrences reported in Table 3.3 is 2088.

The results of the contingency table are analyzed through Heidke Skill Score

(HSS), which is defined as in Nurmi (2003):

$$HSS = \frac{\sum p(f_i, o_i) - \sum p(f_i)p(o_i)}{1 - \sum p(f_i)p(o_i)}, \tag{3.6}$$

where the subscript $i = 4$ denotes the dimension of the table, $p(f_i, o_i)$ represents the combined distribution of radar and disdrometer observations (i.e. the diagonal sum count divided by the total sample size), and $p(f_i)$ and $p(o_i)$ are respectively the marginal probability distributions of the radar and disdrometer observations (i.e. row and column sums divided by the total sum). For the Table 3.3 the HSS has a value of $\simeq 0.1$, which represents a poor result. Although the small number of iced hydrometeors occurrences does not allow statistical inferences, the matching seems particularly low for these hydrometeors. In particular, the main issue is represented by the disdrometer classifications of hydrometeors as liquid particles when the radar classifies the same as solid ones. This mismatch in the liquid/solid classification is even more evident in the third radar elevation classes, where 602 occurrences are classified as snow. The possible causes of this mismatch are mainly two: 1) iced hydrometeors could melt in the path between the position of the radar acquisition and the surface; 2) misclassification of the melting layer position by the radar system, allowing the classification of snow at unlikely heights. The first issue occurs when the freezing level is in the first 1000 m above the surface. As cited in the previous Section, this particular situation results in radar signal scattered back from the melting layer. The second issue is a known problem found in SIMC algorithms.

An example of the first problem is presented in Fig. 3.13, where instruments classifications are showed for an hour between the 23:30 UTC on April 12$^{\text{th}}$ and the 00:30 UTC on April 13$^{\text{th}}$ 2019. Despite the second elevation is not involved

in this event, this example has been chosen because it represents a clear didactic situation. The data of the second radar elevation and disdrometer agree in rain classification for the entire comparison. Conversely, data from the third elevation point out the presence of iced hydrometeors. Available sounding samplings are analyzed to understand if this classification is plausible. Meteorological evidences that underline the possibility of the melting layer located at low heights are observed.

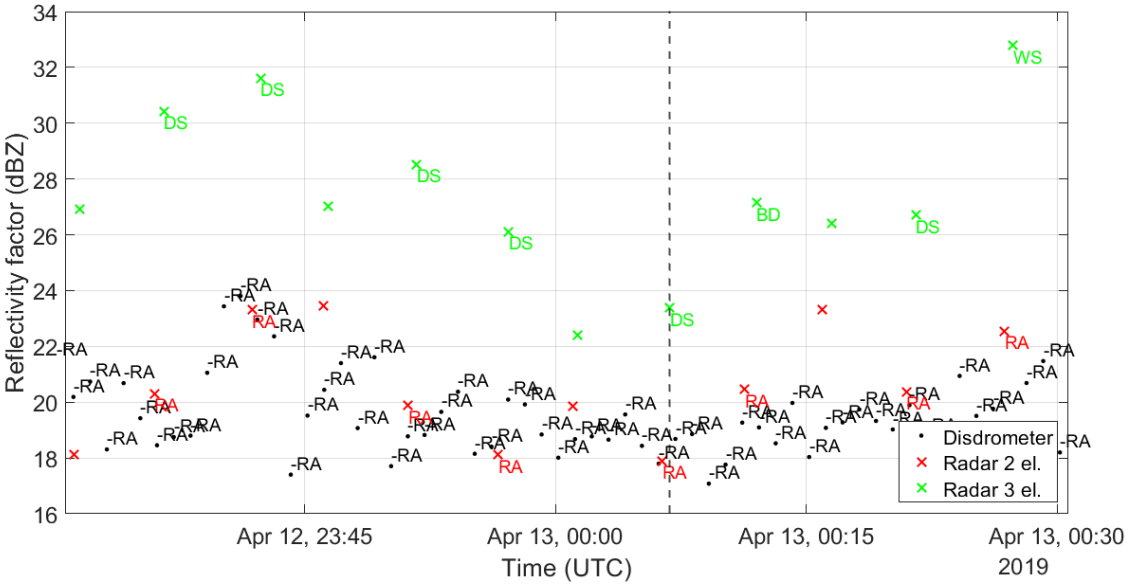

Figure 3.13: Comparison of the reflectivity factors and the instruments classifications of the two instruments. A gray dashed line is placed at the acquisition time of the second elevation (00:05 UTC). Reminder: "RA" - rain (for radar) and moderate rain (for disdrometer); "-RA" - light rain; "DS" - dry snow; "WS" - wet snow; "BD" - big drops.

A cold air mass moving to the Po Valley from east is detected through the analysis of the radio-soundings performed in northern Italy and integrated with the synoptic reanalysis of geopotential height and temperature. Another sounding is available from an airplane departing from the Bologna airport (< 6.5 km from the disdrometer site) few hours after the studied event. This sounding, shown in Fig. 3.14 (a), points

out a temperature close to zero at about 900 hPa, that is just over 1000 m a.s.l.. Since the third radar elevation extends between about 900 m and 1300 m, the frost point is included in the third elevation volume above the city of Bologna.

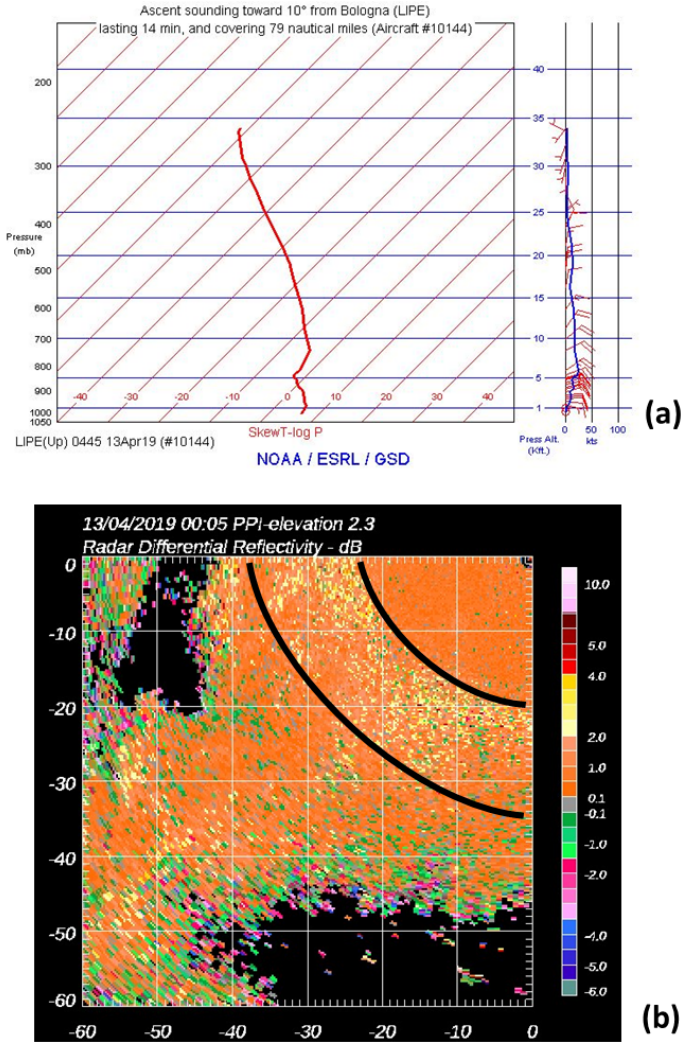

Figure 3.14: Sounding (skewT-logP) collected by an airplane that has been taken off from Bologna Airport "Guglielmo Marconi" on April 13th 2019 at 04:45 UTC, source: amdar.noaa.gov (a); third radar elevation PPI sampled on April 13th 2019 at 00:05 UTC (b); axes values (km) represent the distance from the radar, the colorbar in dB. Black arches identify the melting layer position.

Figure 3.14 (b) shows the PPI of the third elevation Z_{DR} sampled on April 13th 2019

at 00:05 UTC (gray dashed line in Fig. 3.13). A maximum of Z_{DR} is found in the volumes delimited by the two black arches, suggesting the presence of the melting layer. The volume of the third radar elevation cell above the disdrometer is included between the black arches. Therefore, since the melting layer falls into the third radar elevation volume, the radar classification is reasonable. The overestimation of the third elevation Z^{rad} in comparison to the second elevation Z^{rad} and to the Z^{disd} could be caused by the presence of the melting layer (Fig. 3.13).

3.4 Case study thunderstorm (Bologna, 28 may 2019)

On May 28$^{\text{th}}$ 2019 a squall line passed over the city of Bologna,moving toward north-east and generating a severe thunderstorm on the disdrometer site. The evolution of the storm through the area of Bologna is depicted in the sequence of Fig. 3.15, where the disdrometer location (city of Bologna) is at the intersection of the two white lines.

The thunderstorm starts to form southeast of Bologna around 15:30 UTC (first panel of Fig. 3.15) and intensifies in ten minutes (second panel) moving toward north-east (group of red pixel located east of Bologna). The core of the thunderstorm insists on the disdrometer site at 16:00 UTC. This reflectivity maximum is followed by a tail of weaker precipitation that lasts less than an hour. The evolution of the precipitation system is in agreement with the idealized squall line depicted in Fig. 1.3. In fact, the precipitation system is characterized by an intense and localized precipitation structure followed by a lighter and more extended one.

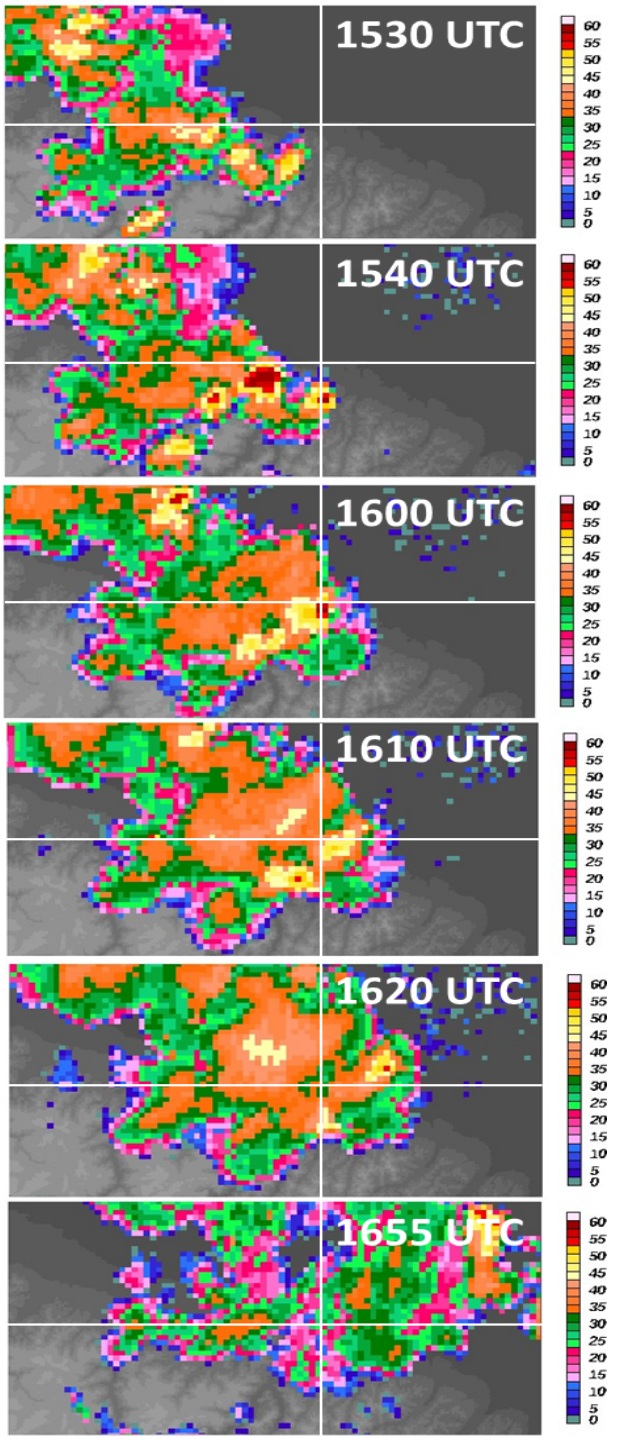

Figure 3.15: Z^{rad} during the evolution of the thunderstorm. Colorbars scale is in dBZ units; Bologna location is identified at the intersection of the two white lines.

3.4.1 Reflectivity comparison

Figure 3.16 shows the values of Z measured by the disdrometer (dashed line) and by the first two radar elevations (red and yellow crosses) during the event.

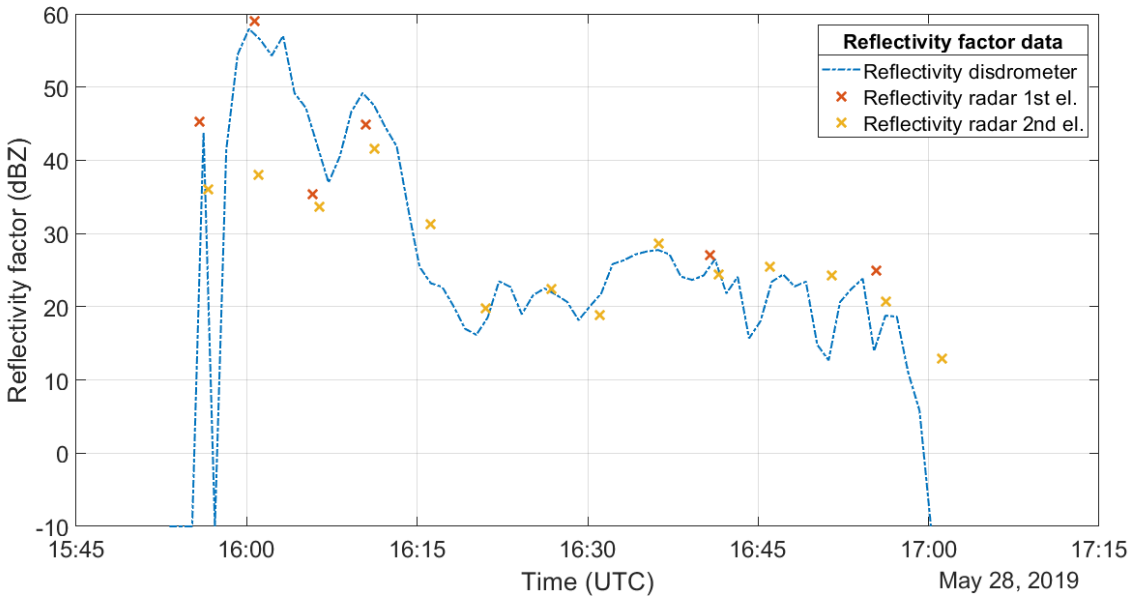

Figure 3.16: Z samplings of the disdrometer and the first and the second radar elevations. Lack of some first radar elevation records is caused by the exclusion of them by the radar filter.

The first part of the event (16:00-16:15 UTC) is characterized by high Z values and by strong conditions of variability, while in the second part (16:15-17:00 UTC) reflectivity settles around 20 dBZ with more homogeneous conditions. The radar samplings follow quite well the disdrometer signal. In fact, especially in the second part of the event, the data of the two instruments match very well. However, in the first section, the second radar elevation does not detect the peak of reflectivity observed by the first elevation and by the disdrometer. Since the high Z values are strongly localized in time, a sampling issue for the radar measurements could

be occurred by missing the minutes of maximum intensity of precipitation. In fact, the radar sampling rate has lower frequency than the disdrometer one. Other issues could be related to the strong spatial localization of the event such as the advection of hydrometeors during the fall. The presence of strong attenuation in the path between the two instruments should be excluded, because in Fig. 3.15 is shown that there are no precipitation structure in radar-disdrometer path.

To understand if the localization of the thunderstorm core could be the cause of the not-detected peak, the 9x9 group of cells centered above the disdrometer of the second radar elevation is studied. The chosen group of cells is in first approximation a box of about 2.5 km in range times 3.6 km in azimuth and 432 m in height.

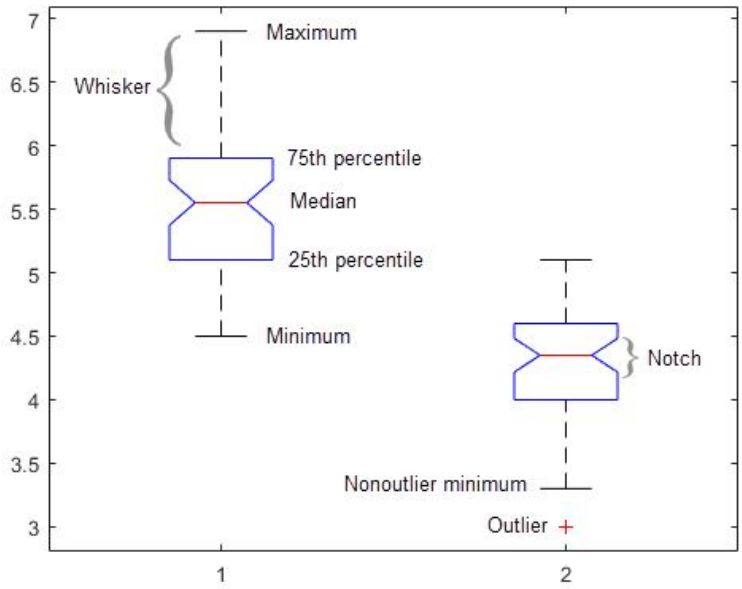

Figure 3.17: Characteristics of a whiskers plot. Source: mathworks.com.

A "whisker plot" is realized trough the 81 values of the group of cells for each acquisition. The characteristics of a whisker plot are described in Fig. 3.17. The edges of the blue box are the 25th and 75th percentiles of the group of cell values.

"Whiskers" are lines extending above and below each box and have a length that goes from the end of the interquartile range (i.e. the difference between 75th and 25th percentiles) to the furthest observation within the whisker length. Whisker length corresponds to a distance that is more than 1.5 times the interquartile range away from the bottom or top of the box; values that fall outside the whiskers interval are labeled as outliers and marked with a red "+" sign. "Notch" represents the display of the variability of the median between samples. Its width is computed so that boxes whose notches do not overlap have different medians at the 5% significance level, assuming a normal distribution.

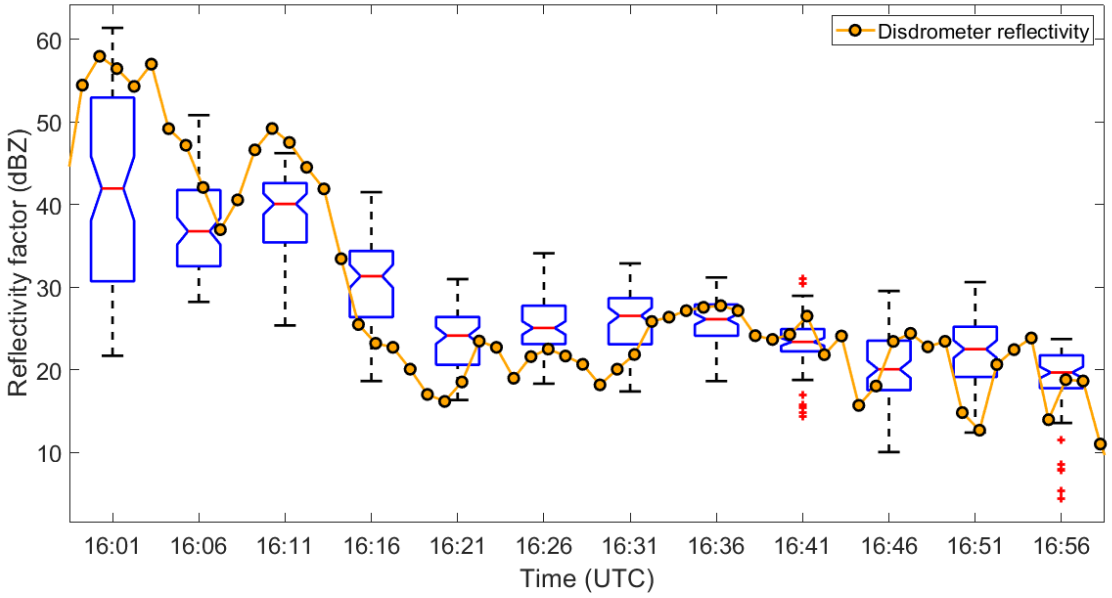

Figure 3.18: Whisker plot of the Z^{rad} of the second radar elevation compared to the disdrometer Z^{disd}. Boxes are plotted at the acquisition time of the second radar elevation.

The whisker plot applied to the event under study is shown in Fig. 3.18, where each box is generated from 81 values. The disdrometer samplings are almost always included in the interval that ranges from the minimum to the maximum

values of the 81 samplings of the group of cells.

Focusing on the 16:01 UTC acquisition, the hypothesis of the advection occurrence of falling hydrometeors is studied. Figure 3.19 shows Z^{rad} of the 9x9 group of cells for the first and the second radar elevations centered on the disdrometer. Comparing the two maps, a shift in the precipitation system between the two elevations seems to be observed. This shift leads to a detection of the storm core by the first elevation, but not by the second one.

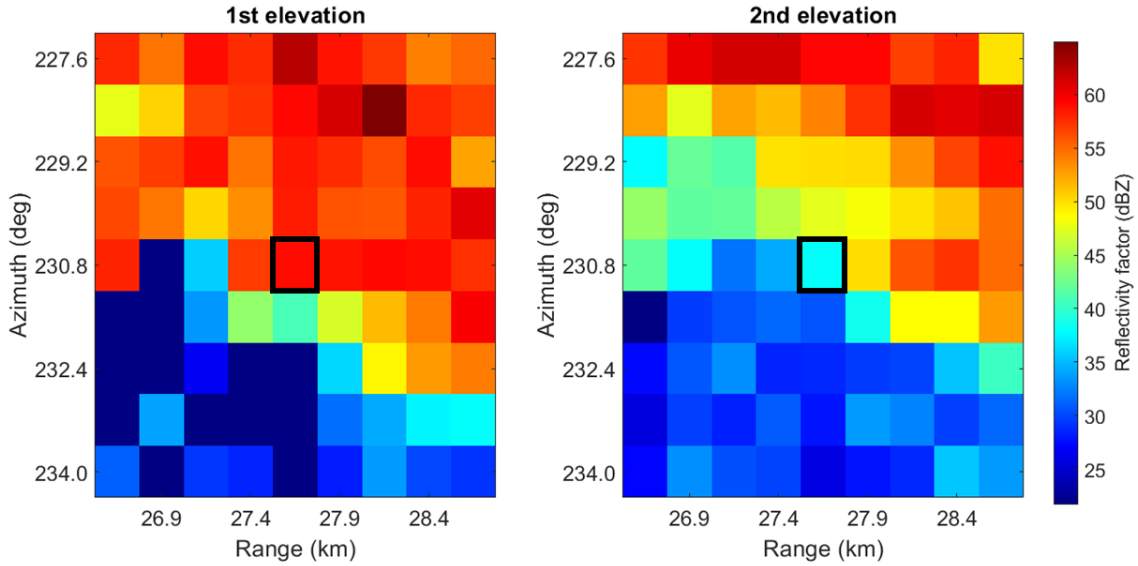

Figure 3.19: Z^{rad} of the 9x9 groups of cells PPIs centered on the disdrometer cell location (identified by black rectangles). On the left, 1st elevation is sampled at 16:00:44 UTC; on the right, 2nd elevation is sampled at 16:01:02 UTC.

An RHI is reconstructed from the Z^{rad} of the first three radar elevations at the disdrometer azimuth. This product is defined "pseudo-RHI" and it is plotted in Fig. 3.20. The shift of the precipitation system observed in Fig. 3.19 is confirmed by the pseudo-RHI: the column of heavier intensity of precipitation is tilted. The oblique shape is a consequence of the system shift in radar direction (toward smaller

ranges), confirmed by the radial velocities retrieved from the radar data. The system moves at a velocity of about 10 ms^{-1}.

This particular situation remarks the importance of having good radar data as close as possible to the ground.

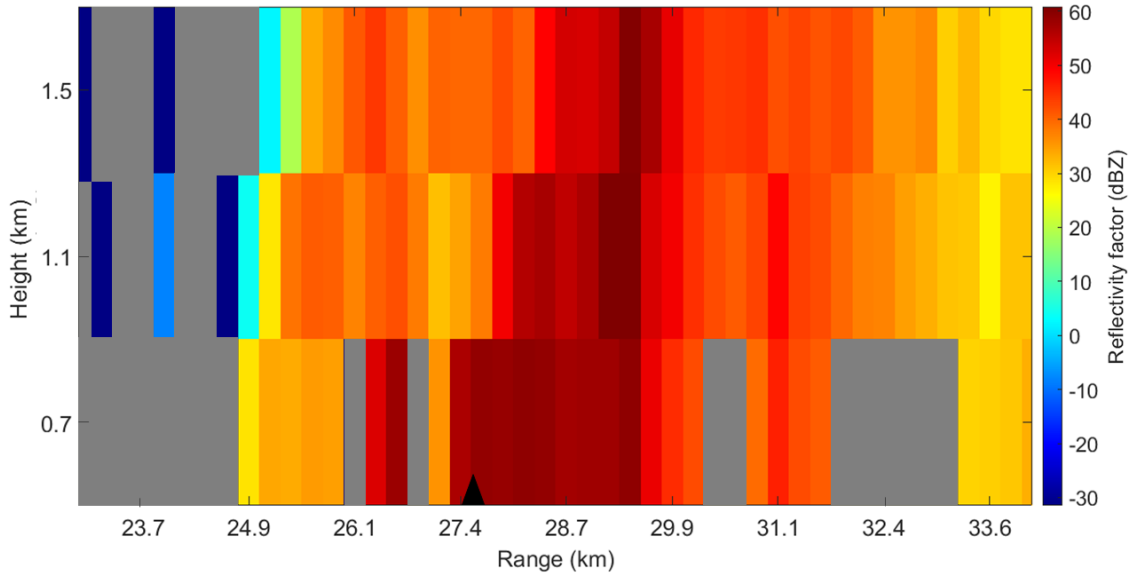

Figure 3.20: Pseudo-RHI reconstructed by merging data of radar elevations 1st to 3rd at the disdrometer azimuth; the radar acquisition starts at 16.00 UTC. Gray boxes represents rejected data by the radar filter. The black triangle is positioned at the disdrometer range.

3.4.2 Disdrometer c/s discrimination and radar polarimetric variables

The effects of the disdrometer classification on the polarimetric quantities of the second radar elevation are analyzed. In particular, the convective/stratiform discrimination applied to the data of the disdrometer is compared with the radar Z_{DR} in Fig. 3.21.

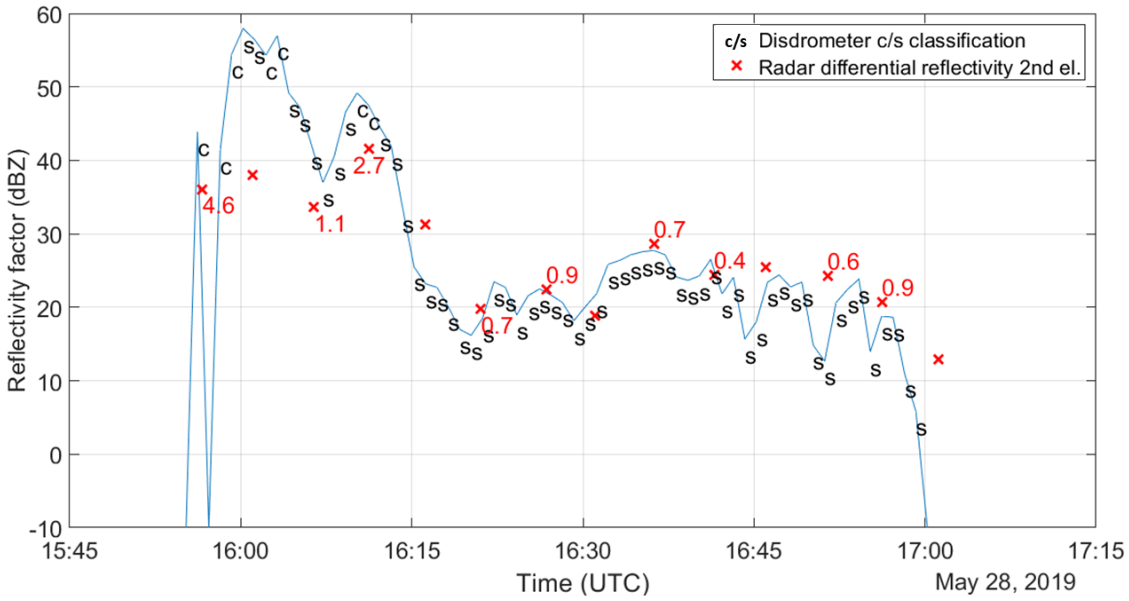

Figure 3.21: Combined analysis of disdrometer convective/stratiform classification and radar differential reflectivity Z_{DR} at the second radar elevation. For the radar scans without a vertical transmitted beam, crosses are without Z_{DR} value.

High Z_{DR} values (>1 dB) are observed in regions of high Z values. This result is plausible because strong precipitation events are related to the presence of large oblate drops. In particular, the 4.6 dB value at 15:56 UTC is a very high value probably associated to large oblate drops in a condition of partially filled radar volume. The radar classification algorithm labels that occurrence as "heavy rain". Figure 3.21 shows that samplings with high Z^{rad} and high Z_{DR} are associated to disdrometer samplings classified as convective.

Quite low Z_{DR} value at 16:06 UTC radar acquisition is directly matched with stratiform occurrences. Considering the high reflectivity factors and the proximity to convective samplings, the hypothesis is that the six stratiform values between the convective ones (16:05-16:10 UTC) have borderline characteristics.

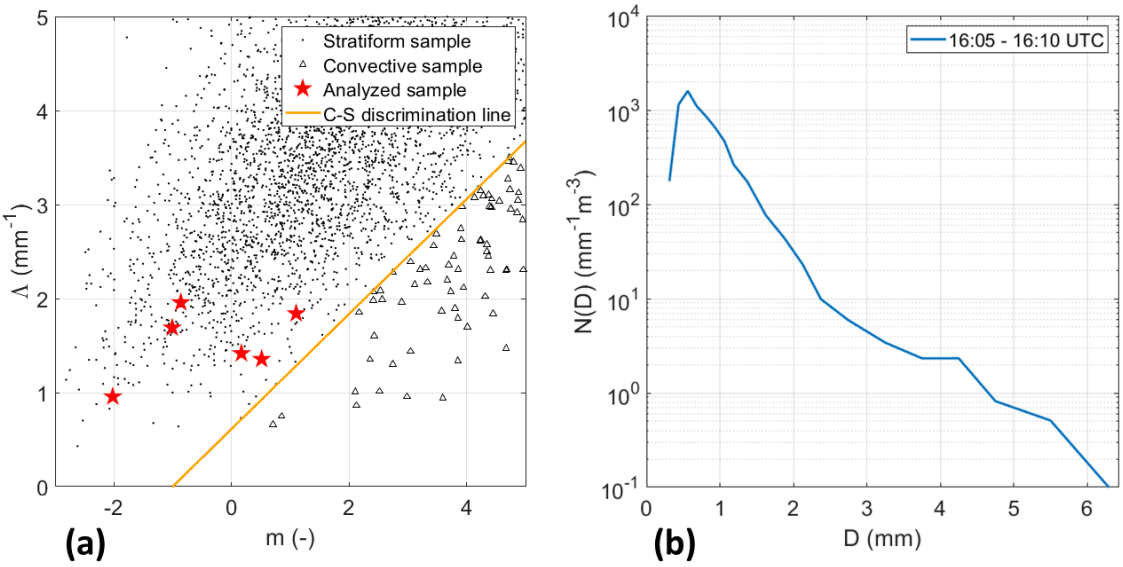

Figure 3.22: Zoom of Fig. 3.8, underlining with red stars the samplings under analysis (16:05-16:10 UTC) (a); six-minutes averaged particle size distribution of the samplings under analysis (b).

To answer to this question Fig. 3.8 (a) is plotted again, highlighting the position of these six samplings under study. The Figure denotes that samplings between 16:05 and 16:10 UTC classified as stratiform are relatively close to the dividing line between the two precipitation patterns; moreover, Caracciolo et al. (2006) observes occurrences of misclassification in case of small m and Λ values. In Fig. 3.22 (b), the 6-min averaged particle size distribution underlines a convective shape of these precipitation samplings due to the presence of large drops (> 4 mm) and of a local maximum at about $4\,mm$.

Referring again to Fig. 3.21, the second radar elevation at 16.11 UTC has an high differential reflectivity value ($Z_{DR} = 2.7$ dB), in fact, it corresponds to a convective sample of the disdrometer. Considering that the third elevation has a relevant lower differential reflectivity value ($Z_{DR} = 1.6$ dB), the following hypothesis

is made: since the radar acquisition is close to a change of the precipitation regime, at the third elevation this change could be already observed.

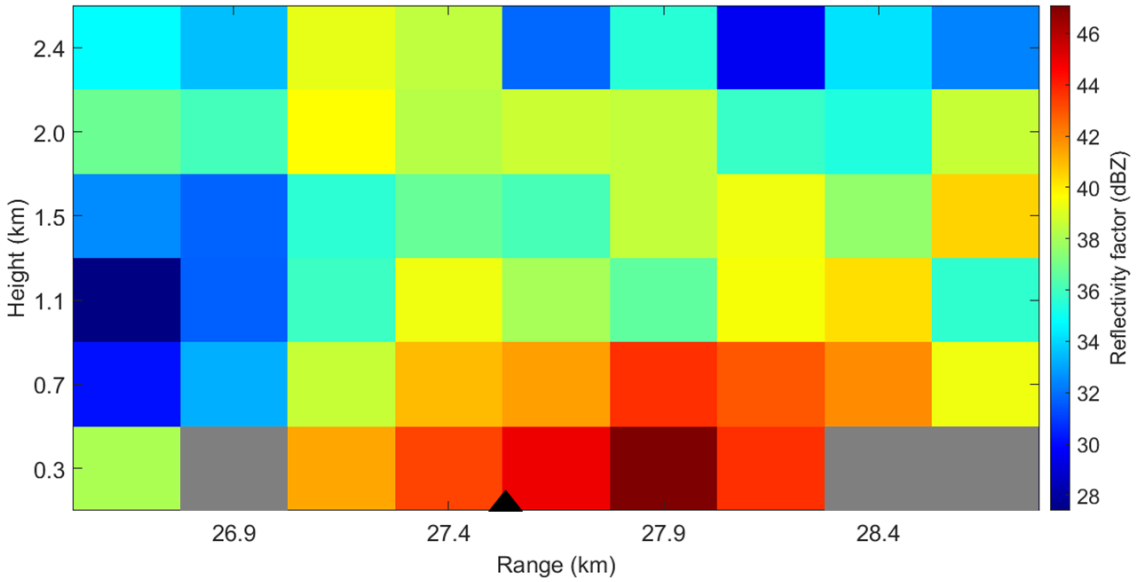

Figure 3.23: Pseudo-RHI reconstructed by merging data of radar elevation 1st to 6th at the disdrometer azimuth; the radar acquisition starts at 16:10 UTC. Gray boxes represents rejected data by the radar filter. The black triangle is positioned at the disdrometer range.

A pseudo-RHI is reconstructed from the Z^{rad} of the first six radar elevations at the disdrometer azimuth. This pseudo-RHI is plotted in Fig. 3.23. Heavy Z^{rad} are observed only at lower elevations. The third radar elevation and the higher ones bring to a considerable underestimation of the precipitation intensities.

In this particular case study, the analysis of the instruments classifications is not performed, because the hailstorm occurred at about 16:00 UTC has not been detected by the radar. In fact, that radar acquisition does not send vertically polarized beam, so the classification of the hydrometeors cannot be generated.

3.4.3 DSD analysis

The analysis of the DSDs in the case study is fulfilled by disdrometer data.

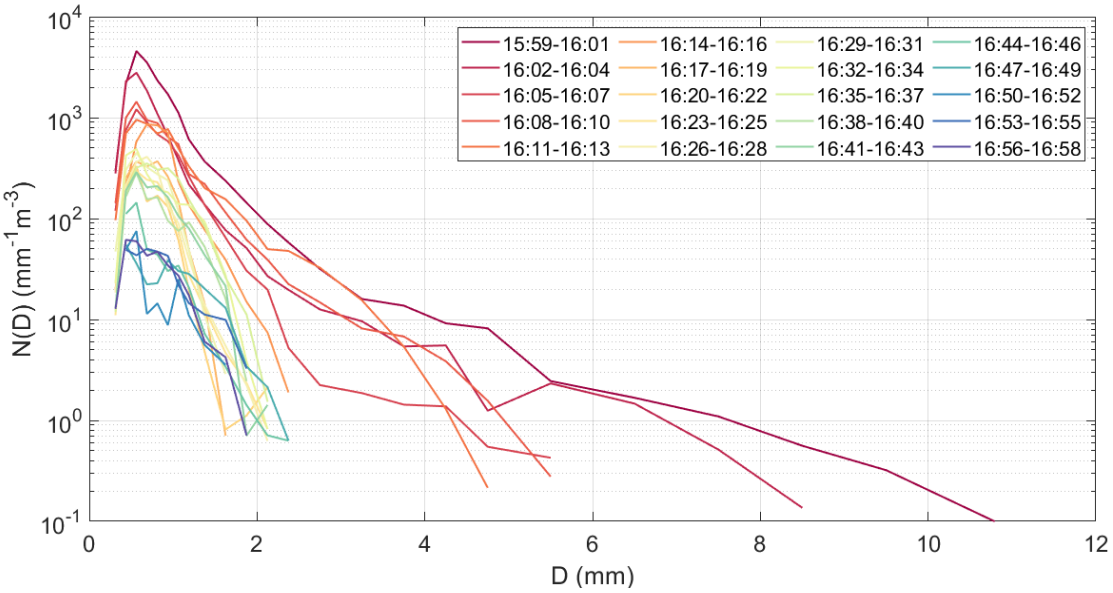

Figure 3.24: Three minute averaged PSD during the case study event. Times in the legend are in UTC.

The evolution of the DSD is shown in Fig. 3.24, where the samples are averaged over three minutes (for reasons of plot readability). Here on, the acronym PSD is used instead of DSD due to the presence of solid hydrometeors. The first minutes are characterized by the convective thunderstorm regime that is underlined by the presence of a significant number of particles with a diameter larger than 4 mm (reddish lines). The following minutes show smaller particle with the largest ones reaching a maximum of about 2 mm (yellow and green lines). In the last part of the event, the residues of the precipitation have distribution shapes that starts to deviate from an exponential parameterization (shades of blue).

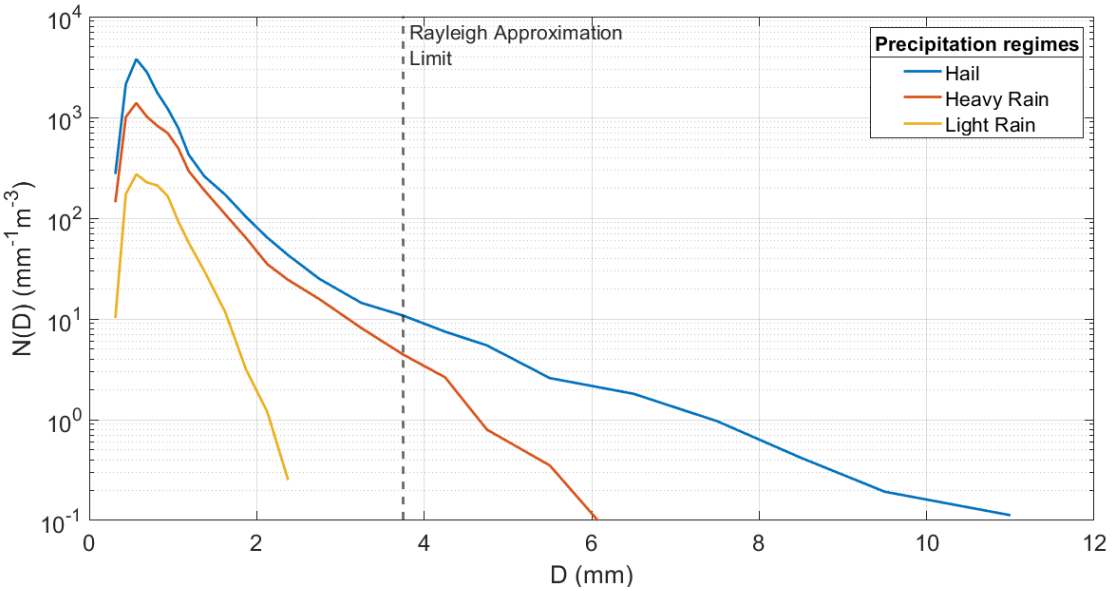

Figure 3.25: PSD characteristics in three different precipitation regimes: hailstorm (15:59-16:03 UTC, blue line), heavy rain (16:04-16:13, red line) and light rain (16:14-16:59, yellow line). The shaded vertical gray line is placed at $D = 3.75\,mm$, which represents the upper validity limit of the Rayleigh approximation.

The precipitation event is divided into three different sections, characterized by three different precipitation regimes:

1. Hail (15:59-16:03 UTC);
2. Heavy rain (16:04-16:13 UTC);
3. Light rain (16:14-16:59 UTC).

During the first section, hailstones up to 1-cm diameter are observed and even in the second section large drops ($> 5\,mm$) are sampled. The first two parts have the typical characteristics of heavy rainfall precipitation occurrences: large drops and a local maximum at about 4 mm (Fig. 1.4 (b)). The third part shows a distribution without local maxima for drops with a diameter larger than 1 mm.

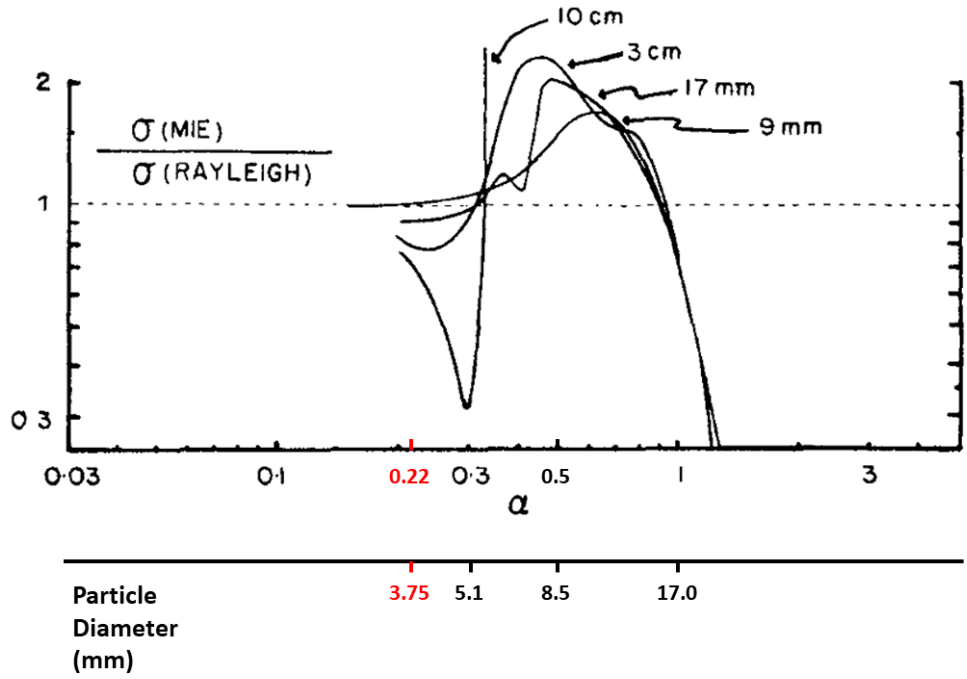

Figure 3.26: Ratio of Mie to Rayleigh backscattering cross sections vs. Mie parameter for beams of various wavelengths. Values of particle diameter were calculated considering a beam with a frequency of 5620 MHz. Red values refers to the threshold above which the Rayleigh approximation is less accurate. Source: edited from Gunn and East, 1954.

The peculiarity of the precipitation patterns no. 1 and 2 is that for particles with a diameter larger than 3.75 mm, the Rayleigh approximation is less accurate in radar measurements (GPM-500C wavelength $\simeq 5.3\,cm$). Since diameters larger of this threshold corresponds to Mie parameters $\alpha > 0.22$ (Eq. 1.30), resonance effects occur as shown in Fig. 3.26. Eq. 1.31 loses its validity as consequence of these effects.

Chapter 4

Conclusions

This Thesis focused on the combined analysis of the data of a weather radar and a disdrometer by characterizing the precipitation and verifying the quality of the radar measurements.

The instruments used for the analysis are a polarimetric C-band radar and a disdrometer PARSIVEL^2. The disdrometer collected data in a sampling surface of about $5.2 \times 10^{-3}\, m^2$ within the city of Bologna, a little less than 28 km far from the radar. The comparison has been carried out choosing the radar sampling volume ($\simeq 47 \times 10^6\, m^3$) above the disdrometer location. The datasets are composed by 11 months of data measured over the years 2019 and 2020.

Four types of analysis have been performed: 1) the comparison of the reflectivity factor data measured by the two instruments; 2) the distributions of the radar variables considering the convective/stratiform discrimination retrieved by disdrometer data; 3) the verification of the operational algorithm of the radar hydrometeor classification in comparison to the disdrometer classification; 4) the investigation of the case study concerning a thunderstorm showing convective and stratiform pre-

cipitation.

The comparison of the reflectivity factor underlined that the first radar elevation is affected by an anthropogenic noise of 20-30 dBZ. Hence, the first elevation has been excluded from the analysis. Then, the data of the second radar elevation of the cell above the disdrometer were compared to the disdrometer data. Since the data of a radar cell are collected almost instantaneously, radar and disdrometer records were matched when the acquisition time of the radar fell into the sampling interval of the disdrometer. The comparison resulted in a good correlation between the instruments, with a correlation coefficient CC=0.84. The radar samplings of the reflectivity factor have a median of 19.3 dBZ, while the disdrometer ones have a median of 18.4 dBZ. This discrepancy may be related to the drifting of particles during the fall, evaporation of falling hydrometeors, the position of the melting layer close to the surface, the different calibration of the instruments and the different spatial extensions of the two domains of the instruments.

Sensitivity analysis has been developed to look for a better matching criterion. This analysis was developed by averaging data measured on groups of radar cells characterized by different extensions (3x3 to 9x9) centered on the disdrometer location. The averaged data were compared to the radar single cell and the disdrometer data. The analysis was repeated by shifting in azimuth and/or in range the data of the single cell that was compared with the disdrometer data. The result showed that the single central cell is statistically the best choice for the matching. However, shifting forward in time the disdrometer data, a slightly better correlations is found. This improvement occurs because the particles observed at the second radar elevation take a certain time to reach the surface.

A “convective” and “stratiform” distribution for each of the radar variables

(reflectivity factor Z^{rad} and differential reflectivity Z_{DR}) were generated, using the discrimination of convective and stratiform precipitation regimes retrieved by the disdrometer. The results show that the convective distributions peak for larger Z^{rad} and Z_{DR} compared to the stratiform ones. Convective distributions have a median of Z^{rad} and Z_{DR} of 34.6 dBZ and 1.5 dB, respectively. The median of Z^{rad} and Z_{DR} are 19.3 dBZ and 0.9 dB for the stratiform distributions. Z^{rad} and Z_{DR} for the regime of convective precipitation are larger because this type of precipitation is characterized by heavier intensities and larger oblate drops than the stratiform one.

Conversely, the radar correlation coefficient ρ_{hv} values are to noisy for make comparisons.

The classification of the hydrometeors type of the two instruments is evaluated through the development of a contingency table. The classifications for the two instruments are divided in 4 classes of the table: rain, heavy rain, hail and snow. The level of correlation between the occurrences in the table is computed through Heidke Skill Score (HSS). The result shows a correlation of about 0.1, which represents a poor result. In particular, an issue is determined by the radar classification of snow hydrometeors when the disdrometer detects liquid ones. The discrepancy could be caused by the incorrect positioning of the melting layer through the radar system and by the melting of hydrometeors in the path between the radar observation and the disdrometer detection.

Then, the case study of a thunderstorm occurred on May 28$^{\text{th}}$ 2019 in Bologna is analyzed. In case of this temporal and spatial localized event the two instruments have discrepancies in reflectivity factor measurements caused by the drifting of particles during the fall. The radar Z_{DR} and the disdrometer convective/stratiform classification are in accordance during this event. However, misclassifications of the

convective/stratiform classification are observed when the precipitation have borderline characteristics between the two patterns.

Finally, the size distribution of particles is analyzed for three different sections of the case study characterized respectively by hail, heavy rain and light rain. Hailstorm and heavy rain sections show significant occurrences of large drops (diameter $D > 4\,mm$) and a local maximum at about $4\,mm$, resulting in the typical shape of convective distributions. Conversely, the section characterized by light intensities shows smaller drops with few occurrences of diameters larger than $2\,mm$.

Further study may be based on the results of this Thesis. A box model could be set up for studying the evolution of DSD into the volume of a radar cell during the fall. This analysis could be an additional verification of the differences between radar and disdrometer calculations. Furthermore, a more rigorous criterion in shifting disdrometer data should be developed. Regarding to the classification of the hydrometeor types, further tests could be performed to improve the correlation between the radar and disdrometer detection of snow. For example, a better positioning of melting layer may be deployed for radar measurements.

Then, the convective/stratiform discrimination algorithm of the disdrometer could be enhanced by using the radar data for borderline regimes of precipitation. Moreover, the effect of the Rayleigh approximation for the larger drops detected by the radar could be investigated.

Bibliography

Alberoni PP, Nanni S, Mezzasalma P, Bech J, Lorente J, Codina B (1998) Dynamic suppression of anaprop conditions, Final report to the European Union on contract No. ENV4-CT96-0261, "DARTH Project". Tech rep

Alberoni PP, Andersson T, Mezzasalma P, Michelson DB, Nanni S (2001) Use of the vertical reflectivity profile for identification of anomalous propagation. Meteorological Applications 8(3):257–266, DOI 10.1017/S1350482701003012

Anagnostou EN, Kummerow C (1997) Stratiform and Convective Classification of Rainfall Using SSM/I 85-GHz Brightness Temperature Observations. Journal of Atmospheric and Oceanic Technology 14(3):570–575, DOI 10.1175/1520-0426(1997)014<0570:SACCOR>2.0.CO;2

Atlas D, Ulbrich CW (1977) Path- and Area-Integrated Rainfall Measurement by Microwave Attenuation in the 1-3 cm Band. Journal of Applied Meteorology 16(12):1322–1331, DOI 10.1175/1520-0450(1977)016<1322:PAAIRM>2.0.CO;2

Babin SM (1996) Surface Duct Height Distributions for Wallops Island, Virginia, 1985-1994. Journal of Applied Meteorology (1988-2005) 35(1):86–93

Battaglia A, Rustemeier E, Tokay A, Blahak U, Simmer C (2010) PARSIVEL Snow

Observations: A Critical Assessment. Journal of Atmospheric and Oceanic Technology 27(2):333–344, DOI 10.1175/2009JTECHA1332.1

Bech J, Codina B, Lorente J, Bebbington D (2002) Monthly and daily variations of radar anomalous propagation conditions: How "normal" is normal propagation? Copernicus GmbH pp 35–39

Bringi VN, Chandrasekar V, Hubbert J, Gorgucci E, Randeu WL, Schoenhuber M (2003) Raindrop Size Distribution in Different Climatic Regimes from Disdrometer and Dual-Polarized Radar Analysis. Journal of the Atmospheric Sciences 60(2):354–365, DOI 10.1175/1520-0469(2003)060<0354:RSDIDC>2.0.CO;2

Caracciolo C, Prodi F, Battaglia A, Porcù F (2006) Analysis of the moments and parameters of a gamma DSD to infer precipitation properties: A convective stratiform discrimination algorithm. Atmospheric Research 80(2-3):165–186, DOI 10.1016/j.atmosres.2005.07.003

Colwell RN (1983) Manual of remote sensing. American Society of Photogrammetry, Falls Church, Virginia

Doviak RJ, Zrnić DS (1993) Doppler Radar and Weather Observations. Dover Publications, Inc., Mineola, New York

Dunkerley D (2008) Rain event properties in nature and in rainfall simulation experiments: a comparative review with recommendations for increasingly systematic study and reporting. Hydrological Processes 22(22):4415–4435, DOI 10.1002/hyp.7045

Dunkerley DL (2010) How do the rain rates of sub-event intervals such as the maximum 5- and 15-min rates (I5 or I30) relate to the properties of the enclosing rainfall event? Hydrological Processes 24(17):2425–2439, DOI 10.1002/hyp.7650

Evans BG (1983) Satellite communications technology. edited by k. miya (k.d.d., japan). k.d.d. engineering & consulting inc., tokyo, japan, 1982. no. of pages: 442. International Journal of Satellite Communications 1(1):60–60, DOI https://doi.org/10.1002/sat.4600010111

Friedrich K, Kalina EA, Masters FJ, Lopez CR (2013) Drop-Size Distributions in Thunderstorms Measured by Optical Disdrometers during VORTEX2. Monthly Weather Review 141(4):1182–1203, DOI 10.1175/MWR-D-12-00116.1

Gunn KLS, East TWR (1954) The microwave properties of precipitation particles. Quarterly Journal of the Royal Meteorological Society 80(346):522–545, DOI 10.1002/qj.49708034603

Gunn KLS, Marshall JS (1958) The Distribution With Size Of Aggregate Snowflakes. Journal of Meteorology 15(5):452–461, DOI 10.1175/1520-0469(1958)015<0452:TDWSOA>2.0.CO;2

Houze Jr RA, Rutledge SA, Biggerstaff MI, Smull BF (1989) Interpretation of Doppler Weather Radar Displays of Midlatitude Mesoscale Convective Systems. Bulletin of the American Meteorological Society 70(6):608–619, DOI 10.1175/1520-0477(1989)070<0608:IODWRD>2.0.CO;2

Joss J, Waldvogel A (1967) Ein Spektrograph für Niederschlagstropfen mit automatischer Auswertung. Pure and Applied Geophysics PAGEOPH 68(1):240–246, DOI 10.1007/BF00874898

Kalina EA, Friedrich K, Ellis SM, Burgess DW (2014) Comparison of Disdrometer and X-Band Mobile Radar Observations in Convective Precipitation. Monthly Weather Review 142(7):2414–2435, DOI 10.1175/MWR-D-14-00039.1

Kinnell P (1976) Some Observations on the Joss-Waldvogel Rainfall Disdrometer. Journal of Applied Meteorology - J APPL METEOROL 15:499–502, DOI 10.1175/1520-0450(1976)015<0499:SOOTJW>2.0.CO;2

Ko HW, Sari JW, Skura J (1983) Anomalous microwave propagation through atmospheric ducts. Johns Hopkins Apl Technical Digest

Komabayasi M, Gonda T, Isono K (1964) Life Time of Water Drops before Breaking and Size Distribution of Fragment Droplets. Journal of the Meteorological Society of Japan Ser II 42(5):330–340, DOI 10.2151/jmsj1923.42.5_330

List R (1958) Kennzeichen atmosphärischer Eispartikeln. Zeitschrift für angewandte Mathematik und Physik ZAMP 9(2):180–192

List R, Nissen R, Fung C (2009) Effects of Pressure on Collision, Coalescence, and Breakup of Raindrops. Part II: Parameterization and Spectra Evolution at 50 and 100 kPa. Journal of the Atmospheric Sciences 66(8):2204–2215, DOI 10.1175/2009JAS2875.1

Löffler-Mang M, Blahak U (2001) Estimation of the Equivalent Radar Reflectivity Factor from Measured Snow Size Spectra. Journal of Applied Meteorology - J APPL METEOROL 40:843–849, DOI 10.1175/1520-0450(2001)040<0843:EOTERR>2.0.CO;2

Löffler-Mang M, Joss J (2000) An Optical Disdrometer for Measuring Size and Velocity of Hydrometeors. Journal of Atmospheric and Oceanic Technology 17(2):130–139, DOI 10.1175/1520-0426(2000)017<0130:AODFMS>2.0.CO;2

Macklin WC, Strauch E, Ludlam FH (1960) The density of hailstones collected from a summer storm. Nubila 3:12–17

Marshall JS, Palmer WMK (1948) The Distribution Of Raindrops With Size. Journal of Meteorology 5(4):165–166, DOI 10.1175/1520-0469(1948)005<0165:TDORWS>2.0.CO;2

Matson RJ, Huggins AW (1980) The Direct Measurement of the Sizes, Shapes and Kinematics of Falling Hailstones. Journal of the Atmospheric Sciences 37(5):1107–1125, DOI 10.1175/1520-0469(1980)037<1107:TDMOTS>2.0.CO;2

McDonald JE (1958) The Physics of Cloud Modification. In: Advances in Geophysics, vol 5, Academic Press Inc., New York, pp 223–303, DOI 10.1016/S0065-2687(08)60079-5

Mitchell DL, Zhang R, Pitter RL (1990) Mass-Dimensional Relationships for Ice Particles and the Influence of Riming on Snowfall Rates. Journal of Applied Meteorology 29(2):153–163, DOI 10.1175/1520-0450(1990)029<0153:MDRFIP>2.0.CO;2

Nurmi P (2003) Recommendations on the verification of local weather forecasts. ECMWF Technical Memorandum 430

OTT (2016) Operating instructions: Present Weather Sensor OTT Parsivel2

Park HS, Ryzhkov AV, Zrnić DS, Kim KE (2009) The Hydrometeor Classifica-

tion Algorithm for the Polarimetric WSR-88D: Description and Application to an MCS. Weather and Forecasting 24(3):730–748, DOI 10.1175/2008WAF2222205.1

Park SG, Kim HL, Ham YW, Jung SH (2017) Comparative Evaluation of the OTT PARSIVEL2 Using a Collocated Two-Dimensional Video Disdrometer. Journal of Atmospheric and Oceanic Technology 34(9):2059–2082, DOI 10.1175/JTECH-D-16-0256.1

Porcù F, D'Adderio LP, Prodi F, Caracciolo C (2013) Effects of Altitude on Maximum Raindrop Size and Fall Velocity as Limited by Collisional Breakup. Journal of the Atmospheric Sciences 70(4):1129–1134, DOI 10.1175/JAS-D-12-0100.1

Prodi F, Tagliavini A, Medini R (2000) Time variability in rainfal events observed by Pludix. Physics and Chemistry of the Earth, Part B: Hydrology, Oceans and Atmosphere 25(10):959–963, DOI https://doi.org/10.1016/S1464-1909(00)00133-7

Pruppacher HR, Beard KV (1970) A wind tunnel investigation of the internal circulation and shape of water drops falling at terminal velocity in air. Quarterly Journal of the Royal Meteorological Society 96(408):247–256, DOI 10.1002/qj.49709640807

Pruppacher HR, Klett J (1997) Microphysics of Clouds and Precipitation, 2nd edn. Kluwer Academic, Dordrecht, Netherlands

Raasch J, Umhauer H (1984) Errors in the Determination of Particle Size Distributions Caused by coincidences in optical particle counters. Particle & Particle Systems Characterization 1(1-4):53–58, DOI 10.1002/ppsc.19840010109

Rinehart RE (1991) Radar for Meteorologists or You, too, can be a Radar Meteorologist. Department of Atmospheric Sciences Center for Aerospace Sciences University of North Dakota, Grand Forks, North Dakota

Rogers RR, Yau MK (1989) A Short Course in Cloud Physics. Elsevier, Burlington, Massachusetts

Rosenfeld D, Ulbrich C (2003) Cloud microphysical properties, processes, and rainfall estimation opportunities. Meteorological Monographs 30:237–237, DOI 10.1175/0065-9401(2003)030<0237:CMPPAR>2.0.CO;2

Smith PL, Liu Z, Joss J (1993) A Study of Sampling-Variability Effects in Raindrop Size Observations. Journal of Applied Meteorology 32(7):1259–1269, DOI 10.1175/1520-0450(1993)032<1259:ASOSVE>2.0.CO;2

Tokay A, Wolff DB, Petersen WA (2014) Evaluation of the New Version of the Laser-Optical Disdrometer, OTT Parsivel2. Journal of Atmospheric and Oceanic Technology 31(6):1276–1288, DOI 10.1175/JTECH-D-13-00174.1

Uijlenhoet R, Sempere Torres D (2006) Measurement and parameterization of rainfall microstructure. Journal of Hydrology 328(1-2), DOI 10.1016/j.jhydrol.2005.11.038

Ulbrich CW (1983) Natural Variations in the Analytical Form of the Raindrop Size Distribution. Journal of Climate and Applied Meteorology 22(10):1764–1775, DOI 10.1175/1520-0450(1983)022<1764:NVITAF>2.0.CO;2

Vittori O, Di Caporiacco G (1959) The density of hailstones. Nubila 2:51–57

Zrnić DS, Keenan TD, Carey LD, May P (2000) Sensitivity Analysis of Polarimetric Variables at a 5-cm Wavelength in Rain. Journal of Applied Meteorology 39(9):1514–1526, DOI 10.1175/1520-0450(2000)039<1514:SAOPVA>2.0.CO;2

Ringraziamenti

A conclusione di questa Tesi, ringrazio il Prof. Federico Porcù che mi ha seguito per la seconda volta come relatore. Oltre alla passione per la meteorologia, una forte motivazione a scegliere questo corso di Laurea è arrivata dallo svolgimento della tesi triennale, scritta proprio con il Professore.

Ringrazio il Dott. Pier Paolo Alberoni che mi ha fatto appassionare alla Radar-Meteorologia e mi ha seguito assiduamente durante la stesura della Tesi, nonostante le difficoltà legate al dover lavorare a distanza.

Un ringraziamento va anche alla Struttura Idro-Meteo-Clima di ARPAE, dove ho ricevuto una bella accoglienza nonostante i pochi giorni di lavoro in presenza.

Ringrazio poi il Dott. Alessandro Bracci che mi ha fornito i dati del disdrometro ed è sempre stato disponibile nei miei confronti.

Ringrazio inoltre la mia famiglia, gli amici di Bologna e di Poggibonsi, che sono il motivo per cui sono una persona felice.